Monthly Notices of the ROYAL ASTRONOMICAL SOCIETY

MNRAS **542,** 1287–1307 (2025) https://doi.org/10.1093/mnras/staf1194
Advance Access publication 2025 August 27

The *JWST*/MIRI view of the planetary nebula NGC 6302 – I. A UV-irradiated torus and a hot bubble triggering PAH formation

Mikako Matsuura [1★] Kevin Volk,[2] Patrick Kavanagh,[3] Bruce Balick [4] Roger Wesson [1,5] Albert A. Zijlstra,[6,7] Harriet L. Dinerstein,[8] Els Peeters [9,10,11] N. C. Sterling,[12] Jan Cami [9,10,11] M. J. Barlow [5] Joel Kastner,[13,14,15] Jeremy R. Walsh,[16] L. B. F. M. Waters,[17,18] Naomi Hirano,[19] Isabel Aleman [20] Jeronimo Bernard-Salas,[21,22] Charmi Bhatt,[9,10] Joris Blommaert,[23] Nicholas Clark,[9,10] Olivia Jones [24] Kay Justtanont,[25] F. Kemper [26,27,28] Kathleen E. Kraemer,[29] Eric Lagadec,[30] J. Martin Laming,[31] F. J. Molster,[32] Paula Moraga Baez,[13] H. Monteiro [1,33] Anita M. S. Richards,[6] Raghvendra Sahai,[34] G. C. Sloan,[2,35] Maryam Torki,[26,27,28] Peter A. M. van Hoof,[36] Nicholas J. Wright [37] Finnbar Wilson[1] and Alexander Csukai[6]

Affiliations are listed at the end of the paper

Accepted 2025 July 16. Received 2025 July 15; in original form 2025 April 4

ABSTRACT

NGC 6302 is a spectacular bipolar planetary nebula (PN) whose spectrum exhibits fast outflows and highly ionized emission lines, indicating the presence of a very hot central star (∼220 000 K). Its infrared spectrum reveals a mixed oxygen and carbon dust chemistry, displaying both silicate and polycyclic aromatic hydrocarbon (PAH) features. Using the *James Webb Space Telescope* Mid-Infrared Instrument and Medium Resolution Spectrometer, a mosaic map was obtained over the core of NGC 6302, covering the wavelength range of 5–28 μm and spanning an area of ∼18.5 arcsec × 15arcsec. The spatially resolved spectrum reveals ∼200 molecular and ionized lines from species requiring ionization potentials of up to 205 eV. The spatial distributions highlight a complex structure at the nebula's centre. Highly ionized species such as [Mg VII] and [Si VII] show compact structures, while lower ionization species such as H^+ extend much farther outwards, forming filament-defined rims that delineate a bubble. Within the bubble, the H^+ and H_2 emission coincide, while the PAH emission appears farther out, indicating an ionization structure distinct from typical photodissociation regions, such as the Orion Bar. This may be the first identification of a PAH formation site in a PN. This PN appears to be shaped not by a steady, continuous outflow, but by a series of dynamic, impulsive bubble ejections, creating local conditions conducive to PAH formation. A dusty torus surrounds the core, primarily composed of large (μm-sized) silicate grains with crystalline components. The long-lived torus contains a substantial mass of material, which could support an equilibrium chemistry and a slow dust-formation process.

Key words: circumstellar matter – ISM: atoms – dust, extinction – ISM: molecules – planetary nebulae: general – planetary nebulae: individual: NGC 6302.

1 INTRODUCTION

Planetary nebulae (PNe) are excellent testbeds for studying the physics and chemistry of photoionized and photondissociated regions (PDRs), which are irradiated by intense ultraviolet (UV) radiation fields. Some central stars of PNe possess dense, dusty tori or discs. Since these stars emit strongly in the UV, PNe containing dusty tori or discs provide opportunities to examine the transition from ionized to neutral and molecular gas within a torus, under varying UV radiation field strength, fast stellar wind, and dust attenuation. These processes are also relevant to star-forming regions and protoplanetary discs. A key advantage of PNe is their large angular extent, allowing them to be spatially resolved with modern telescopes such as the *James Webb Space Telescope* (*JWST*).

Low- and intermediate-mass (1–8 $M_\odot$) evolved stars – asymptotic giant branch (AGB) stars – are an important source of stardust in galaxies (e.g. Dwek 1998; Matsuura et al. 2009a). The processing of this stardust in the interstellar medium (ISM) can be traced by comparing the composition of stardust to that of interstellar dust (Kemper, Vriend & Tielens 2004). It is unclear, however, in what form stardust from AGB stars and their descendants, such as PNe, enters the ISM. This is because (1) evidence is accumulating that their winds have complex, non-spherical structures, such as discs or tori, often associated with binary companions (e.g. Balick & Frank 2002; Sahai, Morris & Villar 2011); (2) it is unclear how freshly made stardust is affected by the harsh UV radiation field or dynamical environment that prevails in PNe (Waters et al. 1998;

★ E-mail: matsuuram@cardiff.ac.uk

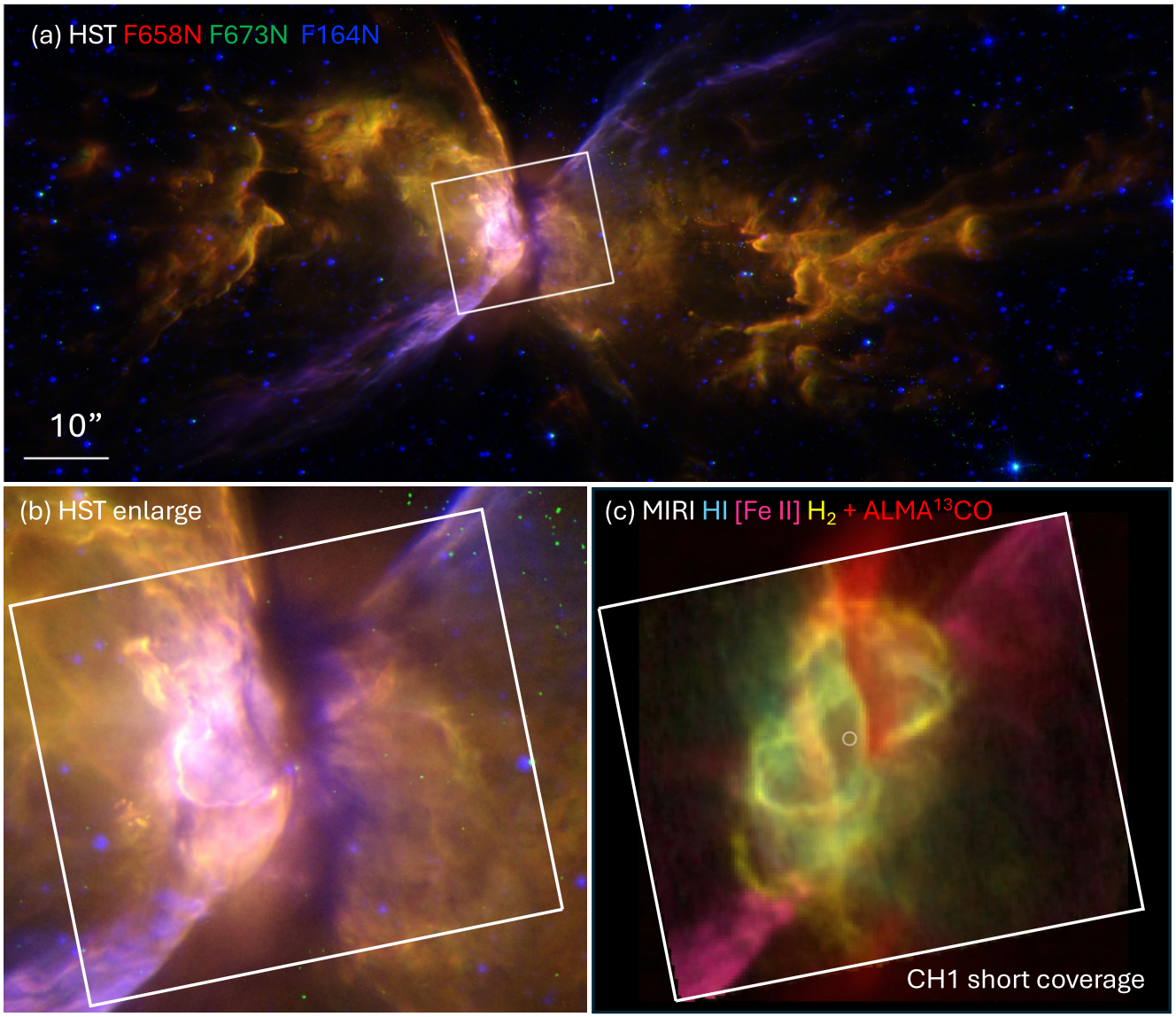

Figure 1. Panel (a): The *JWST*/MIRI mapping area (the white box) of the CH1 short sub-band overlaid on the *HST* three-colour composite image of NGC 6302. North is at the top, and east is to the left. The colour assignments of the *HST*/WFC3 image are *F*164*N* (blue), *F*673*N* (green), and *F*658*N* (red). The *HST* images are from Kastner et al. (2022) and Balick et al. (2023). Panel (b): A zoom-in of the core region of the *HST* image. Panel (c): The same zoom-in of the core region is now shown by features detected with *JWST*/MIRI and ALMA. The MIRI image is composed of H I at 5.907 μm, [Fe II] at 5.34 μm, H_2 at 6.91 μm, and ALMA ^{13}CO 2–1. The white circle marks the location of the central source.

Woods et al. 2003), whose central stars have energetic fast winds and extreme radiation fields (Balick et al. 2023). The presence of the discs and tori could modify the dust grain size and composition by frequent collisions of grains during long time-scale exposures to the UV radiation from the central stars.

The Mid-Infrared Instrument (MIRI)/Integral Field Unit (IFU) spectrometer onboard *JWST* provides an excellent opportunity to probe the composition of gas and dust in heavily UV-irradiated, but also dust-obscured regions, like the tori in bipolar PNe. In order to study extreme chemical and physical conditions, we chose the PN NGC 6302 for our target. This object is one of the most recognizable PNe due to its spectacular bipolar shape (Balick & Frank 2002), displayed in Fig. 1. Based on the first deep optical images obtained of NGC 6302, Evans (1959) described its optical appearance as ‘two lobes of luminous gas, shaped like the wings of a butterfly, separated by a relatively dark lane’, where the dark lane is the dusty torus (Lester & Dinerstein 1984; Matsuura et al. 2009b). It has one of the highest estimated initial masses (5–6 $M_\odot$) and the hottest central star (220 000 K) of any Galactic PN, with high nitrogen abundance, making it a rare PN descended from an intermediate-mass star (Wright et al. 2011).

One of the important characteristics of NGC 6302 is the presence of both oxygen-rich and carbon-rich dust within a single object. Once formed and ejected, CO molecules lock up C and O atoms. Depending on the C/O abundance ratio, an excess of C atoms forms carbon-bearing molecules and dust, such as polycyclic aromatic hydrocarbons (PAHs), while an excess of O atoms forms oxygen-rich molecules and dust, such as silicates. Both crystalline silicates and PAHs are detected in NGC 6302, amid an O-rich gas chemistry (C/O $\sim$ 0.4; Wright et al. 2011). It has been hypothesized that the

crystalline silicates formed in the dusty torus (Waters et al. 1998; Molster et al. 1999), where the high density and strong UV irradiation enabled slow annealing of dust grains or dust processing over long time-scales ($\sim 10^5$ yr; Molster et al. 1999), but this hypothesis has yet to be confirmed.

We present *JWST* MIRI IFU mapping of the core of NGC 6302, allowing a detailed morphological snapshot of atomic lines, H_2, PAHs, and crystalline silicate components. The MIRI IFU map reveals the stratification of ionized gas in a bubble: atomic lines with higher ionization potential are emitted in a compact region, while lines with lower ionization potential are more extended. H_2 is found in arc-like filaments at slightly larger radii. These new *JWST* spatio-kinematic 3D maps capture for the first time how PAHs and crystalline silicates form, in a spatially resolved manner. The detection of the central source is reported in a separate paper (Wesson et al., in preparation).

2 TARGET: NGC 6302

NGC 6302 is among the best-studied PNe. It exhibits extreme bipolar, complex morphology, the presence of very high excitation gas, high molecular mass, and crystalline silicate dust (Molster et al. 2001; Balick & Frank 2002; Peretto et al. 2007; Kastner et al. 2022). In the optical and near-infrared (IR) *Hubble Space Telescope* (*HST*) images (Fig. 1), the central region displays a torus, most of which is highly obscured by dust (Kastner et al. 2022). It has been suggested that this torus has confined more recent gas and dust ejections from the original AGB central star, now the PN central star, and shaped the bipolar nebula (Balick & Frank 2002).

This torus contains a substantial mass of gas and dust, and is slowly rotating (<0.1 km s^{-1}) as it expands (~ 10 km s^{-1}; Rodriguez & Moran 1982; Dinh-V-Trung et al. 2008; Santander-García et al. 2016). The total torus mass is estimated to be ~ 2 M$_\odot$ from CO lines (Peretto et al. 2007), with 0.03 M$_\odot$ of dust (Matsuura et al. 2005).

NGC 6302 is a luminous PN (total luminosity of $\sim 14\,000$ L$_\odot$; Wright et al. 2011). Analysis of the nebular atomic lines shows that the central star is one of the hottest among PNe (Ashley & Hyland 1988), with an approximate effective temperature of 220 000 K (Wright et al. 2011). The central star that provides such a large energy has so far not been directly detected. Matsuura et al. (2005) suggested that a IR point source was the central star, but Szyszka et al. (2009) argued that a faint optical star, located at the very centre but different from the IR point source, was the central star. Later, this optical star was found to be a foreground star with high proper motion, therefore not the central star (Kastner et al. 2022). The true central star appears to be hidden by dust extinction or blinded by strong emission from ionized gas at optical wavelengths.

The nebula itself shows a complex morphology, with several pairs of long bipolar lobes with slightly different axes and ages (Balick & Frank 2002; Balick et al. 2023). Fig. 1 shows a *HST* optical and near-IR composite image. The bright butterfly wings of the bipolar nebula extend over 1 arcmin (Kastner et al. 2022; Balick et al. 2023). However, fainter nebulosity stretches (end-to-end) as far as 7 arcmin (Meaburn et al. 2005; Pignata et al. 2024), corresponding to a linear diameter of 2.1 pc at a distance of 1.03 ± 0.27 kpc (Gómez-Gordillo et al. 2020). Expansion measurements have indicated that these lobes were ejected 2250 yr ago, post-dating the ejection of the torus (Szyszka, Zijlstra & Walsh 2011). Balick et al. (2023) identified at least five other younger mass ejections within these wings

The origin of such a complex nebula is controversial. Wright et al. (2011) model it as a single star evolving on a post-AGB track. In contrast, Soker & Kashi (2012) include it as an intermediate-luminosity optical transient (such as a red nova) that evolved through an explosive event. Uscanga et al. (2014) model the structure with interacting winds but found that additional acceleration is required. Balick et al. (2023) point out that no ejection scenario accounts for the recurrent outbursts at diverse angles. Resolving this will require identifying the central star and possible companion stars.

2.1 Distance and foreground extinction

As the central star of NGC 6302 is not detected in the optical, its distance measurements rely on methods other than optical parallax. From expansion measurements, Meaburn et al. (2005) derive a distance of 1.04 ± 0.16 kpc, improved to 1.17 ± 0.14 kpc by Meaburn et al. (2008). A similar method was applied by Gómez-Gordillo et al. (2020), resulting in a distance estimate of 1.03 ± 0.27 kpc. We adopt this distance.

NGC 6302 lies near the Galactic plane ($b = 1.0557$), hence may suffer from significant foreground ISM extinction. The foreground extinction is estimated to be $c(H\beta) = 0.78 \pm 0.10$ (Rauber, Copetti & Krabbe 2014), corresponding to $E(B-V) = 0.53 \pm 0.07$ mag.

3 OBSERVATIONS AND DATA REDUCTION

3.1 Observations

We observed NGC 6302 with *JWST* (Gardner et al. 2023) in Cycle 1 General Observers (GO) program 1742 (PI: Matsuura). The data were acquired on 2023 September 9, using the MIRI Medium Resolution Spectrometer (MRS; Wells et al. 2015; Argyriou et al. 2023) with IFU (Wright et al. 2023). The full spectral coverage of 4.9–27.9 μm was obtained with four different channels (CH1–CH4) (Table 1).

A mosaic map of 5 × 5 tiles was used to cover the heart of NGC 6302 (Fig. 1). The mapping covers approximately 18.5 arcsec × 15.5 arcsec (CH1 short) to 22.9 arcsec × 19.3 arcsec (CH4 long) with increasing areas at longer wavelengths. The mapping centre was defined as RA 17:13:44.3938 and Dec. −37:06:12.36 (J2000), though the actual centres of the maps have slight (a few tenths of arcsec) differences among channels, due to differences in the dithered positions. The observations were carried out using a four-point dither pattern, which is optimized for an extended object. The exposure time per sub-band and per tile was 111–255 s (Table 1), and the readout pattern of FASTR1 was used.

Because the MIRI MRS observations can contain substantial emission from the zodiacal light and telescope thermal emission, the 'background' was measured at the offset sky position at RA 17:13:30.66 and Dec. −37:04:23.4 (J2000), and subtracted from the target data. The number of groups was the same as the target, with the readout pattern of FASTR1. The dither 1 was chosen with a total of two dithers for each, optimized for a point source mode. The total integration was 2 s for the background, making the total exposure times of 55.5, 88.8, and 127.7 s for short, medium, and long sub-bands.

The pointing accuracy was evaluated based on two field stars within the MIRI mapping area: one on the east and the other on the west. The western star has a *Gaia* Data Release 3 (DR3) identification as *Gaia* DR3 5973805626168712320, with a proper motion of $\mathrm{pm_{RA}} = -1.071$ mas yr^{-1} and $\mathrm{pm_{Dec.}} = -7.487$ mas yr^{-1} (Gaia Collaboration 2023). With about a 6.5-yr difference between

Table 1. *JWST*/MIRI observations of NGC 6302.

Channel	Slice width (arcmin)	Pixel size (arcmin)	Sub-band	Wavelength (μm)	R	PSF (arcmin)	t_{exp} (s)	Map size (arcmin)
CH1	0.177	0.196	Short	4.9–5.74	3320–3710	0.27–0.30	111	15.5 × 18.2
			Medium	5.66–6.63	3190–3750	0.29–0.32	178	15.5 × 18.2
			Long	6.53–7.65	3100–3610	0.32–0.36	255	15.4 × 18.2
CH2	0.280	0.196	Short	7.51–8.77	2990–3110	0.35–0.40	111	16.1 × 19.1
			Medium	8.67–10.13	2750–3170	0.39–0.44	178	16.1 × 19.3
			Long	10.02–11.70	2860–3300	0.44–0.49	255	16.2 × 19.4
CH3	0.390	0.245	Short	11.55–13.47	2530–2880	0.49–0.55	111	17.7 × 20.4
			Medium	13.34–15.57	1790–2640	0.55–0.62	178	17.9 × 20.6
			Long	15.41–17.98	1980–2790	0.61–0.70	255	17.5 × 20.4
CH4	0.656	0.273	Short	17.70–20.95	1460–1930	0.69–0.80	111	19.2 × 22.2
			Medium	20.69–24.48	1680–1770	0.79–0.91	178	19.2 × 22.2
			Long	24.19–27.9	1630–1330	0.90–1.03	255	18.9 × 22.2

Note. The MIRI instrumental design and capabilities, including the FWHM of the PSF (Argyriou et al. 2023). The exposure time (t_{exp}) and the approximate map size are specific to this program after the final data reduction.

the *Gaia* and MIRI observations, the proper motion of this star is about 0.05 arcsec. Compared with the angular resolution of MIRI (0.36–0.4 arcsec in full width at half-maximum (FWHM) in CH1; Argyriou et al. 2023), this proper motion is negligible.

The eastern star does not have a *Gaia* DR3 identification but is identified as the VISTA source VVV (VISTA Variables in the Vía Láctea) J171344.99−370615.59 (Saito et al. 2012). The coordinates of these two stars were compared with those from the *HST F160W* image (Kastner et al. 2022), which was astrometrically calibrated using the coordinates of multiple field stars with *Gaia* DR3 entries. The differences (MIRI − *HST*) of the coordinates are 0.005 arcsec in the RA direction and 0.05 arcsec in the Dec. direction for the eastern star and −0.009 arcsec in the RA direction and 0.08 arcsec in the Dec. direction for the western star. This is consistent with *JWST*'s positional/pointing accuracy of <0.1 arcsec (Rigby et al. 2023).

3.2 Data reduction

To reduce the MRS data, we used a development version of v1.14.0 *JWST* Calibration Pipeline (Bushouse et al. 2023) with versions 11.17.16 and 'jwst_1202.pmap' of the Calibration Reference Data System (CRDS) and CRDS context, respectively. We processed all level 1b (ramp) files through the `Detector1Pipeline` to produce level 2a (rate) images. Using the dedicated background exposures, we generated master background images for each MIRI/MRS sub-band and subtracted these from the science exposures. The resulting background-subtracted level 2a files were processed through `Spec2Pipeline`, with the `residual_fringe` step switched on to produce flux-calibrated level 2b (cal) images. These were then processed through `Spec3Pipeline` to produce spectral cube mosaics of NGC 6302 in all 12 MIRI/MRS sub-bands by setting the `cube_build` parameter 'output_type' to 'band'.

3.3 The integrated MIRI spectrum

Spectra were extracted from each of the MIRI/MRS sub-band mosaic cubes using the `aperture` module in the ASTROPY PHOTUTILS package[1] (Bradley et al. 2022). We applied the additional post-pipeline residual fringe correction to all our spectra, which is included in the *JWST* Calibration Pipeline package under the `extract_1d` step. The integrated spectra were extracted from a large (5 arcsec at 5.5 μm) aperture enclosing the central bright emission region through the MRS spectral channels. The aperture was allowed to 'grow' slightly with increasing wavelength to account for the effect of the increasing MIRI point spread function (PSF). This ensured a consistent extraction region across the full spectral range of the MRS and that scaling of the spectral sub-bands was not required. This integrated MIRI spectrum is shown in Fig. 2. It shows many lines, superposed on dust and PAH features.

The spectra are affected by many issues resulting from the very bright and/or saturated emission lines from NGC 6302. Saturated lines are flanked by faint emission features on either side, caused by scattered light. In the case of the 10.52 μm [S IV] line, these are seen across a range of 0.1 μm, while the 7.65 μm [Ne VI] line shows wings from scattered light over a 0.2 μm width. Strongly saturated lines can also cause negative artefacts (seen at 5.5 μm, for instance), which vary across the field and result from the column/row pull-up/pull-down effect. Finally, strong lines can cause cross-talk with other spectral segments. This is seen, for instance, at 6.8–6.88 μm, where a weak bump in the spectrum is caused by cross-talk from the saturated 10.52 μm line. This results from light scattering into the neighbouring channel. These effects are described in more detail in Argyriou et al. (2023). We identified all potential detector artefacts through careful inspection of all level 2b images, data cubes, and spectra, which were taken into account in our analysis and interpretation. Due to the impact of the bright/saturated lines on the shape of the continuum, we did not perform any scaling of the individual sub-band spectra.

3.4 Ancillary data

We use ^{13}CO J = 2–1 and H30α data at 231.90 GHz from the Atacama Large Millimeter/submillimeter Array (ALMA) project 2012.1.00320.S (PI: Hirano). This project obtained 12-m interferometric data of NGC 6302 with array configurations of C32-4 on 2014 March 9. The central ∼50 arcsec region, including the torus, was covered with the seven-pointing mosaic mode. The bandpass, phase, and flux calibration sources were J1700−2610, J1720−3552, and Titan, respectively. This project further observed NGC 6302 with the Atacama Compact Array (ACA) 7-m array and the Total Power (TP) Array. The 7-m array observations were conducted during the period from 2013 October 6 to 2014 March 22, and the TP observations were taken in 2015 July between the 22nd and 24th. The total integration

[1] https://photutils.readthedocs.io/en/stable/

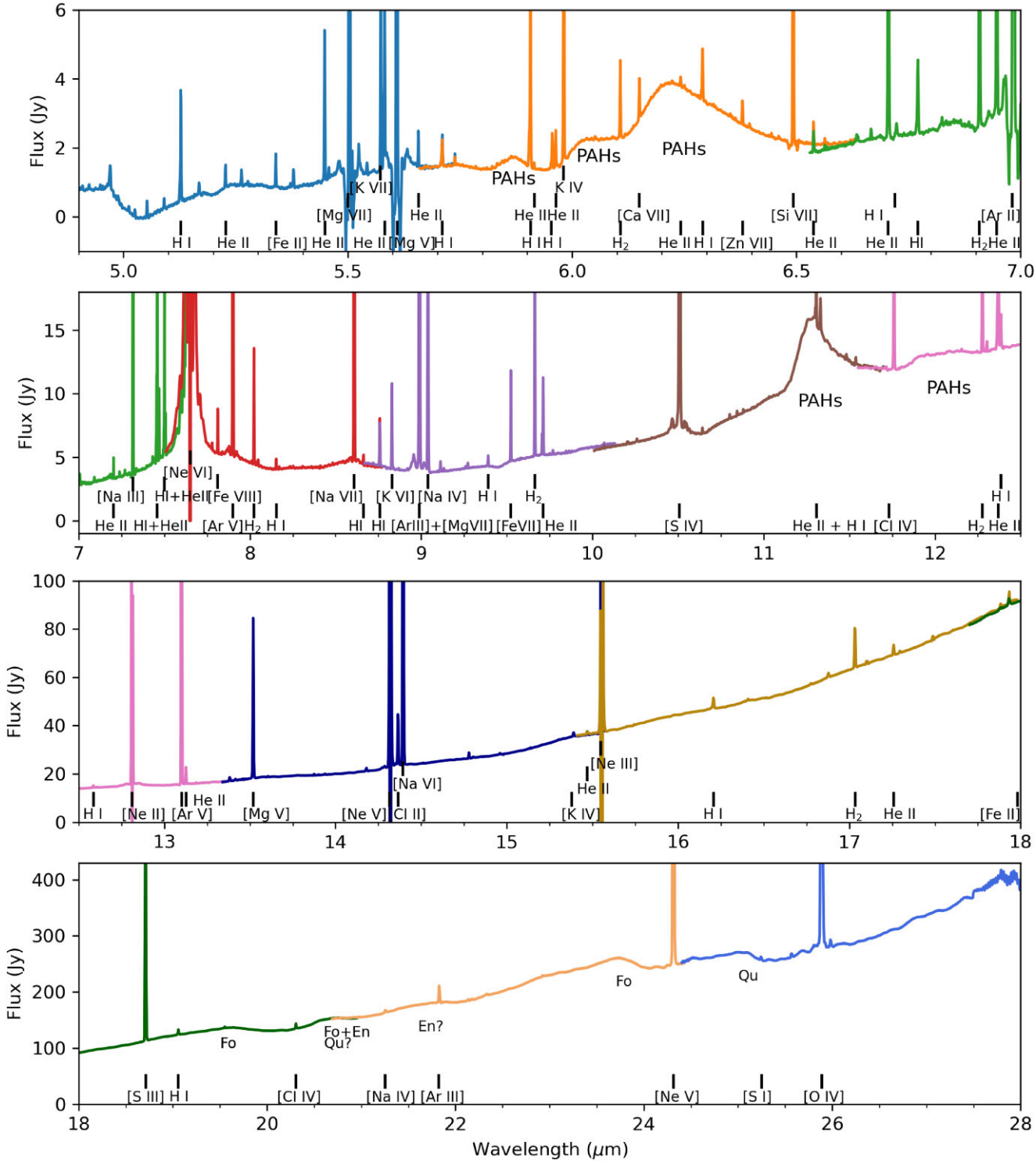

Figure 2. The integrated spectra of NGC 6302 within the MIRI mapped area. Different colours are used to indicate different grating orders of MIRI. Representative identifications of lines and dust features are labelled. The labels of crystalline dust are: Fo (Forsterite), En (Enstatite), and Qu (Quartz). Some bright atomic lines saturated the detectors, and their line profiles can show negative excursions.

time on source was 98.6 min for the 12-m array, 75 min for the 7-m array, and 276.5 min for the TP.

In post-processing, the 12-m, 7-m, and TP data are combined using casa (CASA Team 2022), with the beam size of 0.76 arcsec × 0.66 arcsec (major and minor axes) with the position angle of −0.89°.

4 ANALYSIS AND RESULTS

4.1 Spectral features

The integrated MIRI spectrum of the whole field shows a wealth of narrow gas emission lines, broad emission features from PAHs, and

a dust continuum. The identifications of representative atomic lines, PAHs, and dust features are labelled in Fig. 2.

4.1.1 Emission lines

The line fitting code ALFA (Wesson 2016) was used to measure the central wavelength and flux of each emission line. A total of 142 lines were measured with ALFA. Line fluxes were also manually measured using IDL routines that integrate above a user-defined continuum, and perform simultaneous multicomponent Gaussian fits to blended features. The direct measurements are particularly valuable for obtaining accurate fluxes of weak features and of those in regions of rapidly varying continuum, e.g. on broad PAH or dust features. An additional 36 lines were measured in this manner, for a total of 178 detected lines.

To identify features, initial line lists were compiled from the Beintema & Pottasch (1999) *Infrared Space Observatory* (*ISO*)/Short Wavelength Spectrometer (SWS) 2.4–36 μm spectrum of NGC 6302, and the *JWST*/MIRI spectra of the Ring Nebula (NGC 6720) reported by Wesson et al. (2024) and van Hoof et al. (in preparation). Because the central star of NGC 6302 has a higher effective temperature (220 000 K) than that of NGC 6720 (130 000 K), it is expected to exhibit emission from more highly ionized species.

Line identifications were determined based on wavelength, ionization potential, and morphology (as described in Section 4.4). Wavelengths and ionization potentials for atomic features were obtained from CHIANTI (Dere et al. 2023), NIST,[2] the Atomic Line List (van Hoof 2018),[3] and the *ISO*/SWS spectral list assembled by Peter van Hoof.[4] The wavelengths of H_2 lines were taken from Roueff et al. (2019). Of the detected lines, 66 are identified as H I, 54 as He II, 8 are H_2 lines, and the remainder are forbidden lines (Table 2).

We detect numerous lines from very high ionization species that are referred to as 'coronal lines' (Greenhouse et al. 1990, 1994).[5] For example, MIRI detected a [Si VII] 6.49 μm line. This ion is also seen in the near-IR spectrum (Ashley & Hyland 1988), and requires photon energies of 205.3 eV to form. Additionally, transitions from several ions that require 120–190 eV to produce were detected (Table 3), including [Mg VII], [Al VI], and [Cr IX].

The measured line fluxes integrated over the full MRS mapping area are more or less consistent with those measured with *ISO*/SWS (Beintema & Pottasch 1999). The *ISO*/SWS had aperture sizes from 14 arcsec × 20 arcsec (at 5 μm) to 20 arcsec × 27 arcsec (at 28 μm). Despite the different SWS aperture sizes and MIRI mapping area, these consistent measurements show that the majority of the mid-IR line fluxes originate from this central region of the PN.

Strong lines that saturated the MIRI detectors are [Mg VII] at 5.493 μm, [Mg V] at 5.610 μm, [Ar II] at 6.985 μm, [Ne VI] at 7.652 μm, [Ne II] at 12.814 μm, and [Ne V] at 14.322 μm.

[2]https://www.nist.gov/pml/atomic-spectra-database
[3]https://linelist.pa.uky.edu/newpage/
[4]https://www.mpe.mpg.de/ir/ISO/linelists/index.html
[5]These ions are seen in the Sun's corona, where they are understood to be produced under collisional ionization equilibrium at gas temperatures of $\sim 10^5$–10^6 K. In current astronomical usage, for example, as seen in classical novae and AGN, 'coronal lines' arise from ions that require ionization energies of ≥ 100 eV (Greenhouse et al. 1994). In other astronomical sources, such as PNe, novae, these ions may alternatively be produced by high-energy photons, as appears to be the case in NGC 6302.

Table 2. Emission line fluxes (10^{-12} erg cm^{-2} s^{-1}) measured in the integrated MRS spectrum of NGC 6302.

λ_{obs} (μm)	λ_{rest} (μm)	Flux	Species
4.9084	4.9088	0.020 ± 0.005	He II 28–13
4.9236	4.9237	0.024 ± 0.003	H I 23–7
4.9532	4.9541	0.020 ± 0.004	H_2 1–1 S(9)
4.9699	4.9709	0.272 ± 0.046	H I 22–7 + [Ni I]
5.0124	5.0126	0.032 ± 0.008	He II 27–13
5.0252	5.0261	0.060 ± 0.008	H I 21–7
5.0524	5.0531	0.110 ± 0.008	H_2 0–0 S(8)
5.0908	5.0913	0.069 ± 0.009	H I 20–7
5.1257	5.1266	0.146 ± 0.015	He II 20–12
5.1279	5.1287	0.793 ± 0.027	H I 10–6
5.1684	5.1693	0.058 ± 0.004	H I 19–7
5.2276	5.2280	0.139 ± 0.016	He II 16–11
5.2629	5.2637	0.083 ± 0.017	H I 18–7
5.2772	5.2777	0.018 ± 0.005	He II 25–13
5.3396	5.3402	0.168 ± 0.014	[Fe II]
5.3725	5.3736	0.021 ± 0.003	[Fe II]
5.3791	5.3798	0.104 ± 0.010	H I 17–7
5.4484	5.4480	0.768 ± 0.031	He II 24–13 + [Fe VIII]
5.4580	5.4583	0.023 ± 0.004	He II 19–12
5.5036	5.4927	Saturated	[Mg VII]
5.5244	5.5252	0.078 ± 0.027	H I 16–7
5.5732	5.5748	0.857 ± 0.065	[K VI]
5.5799	5.5806	0.363 ± 0.067	He II 13–10
5.5821	5.5828	0.763 ± 0.062	He II 11–9
5.6092	5.6098	Saturated	[Mg V]
5.6575	5.6582	0.166 ± 0.009	He II 23–13
5.7080	5.7091	0.032 ± 0.004	He II 30–14
5.7106	5.7115	0.148 ± 0.016	H I 15–7
5.7852	5.7870	0.009 ± 0.002	[Cr IX]
5.8100	5.8109	0.005 ± 0.001	H_2 1–1 S(7)
5.8220	5.8227	0.005 ± 0.001	He II 29–14
5.9046	5.9058	0.181 ± 0.041	He II 18–12
5.9073	5.9082	1.019 ± 0.041	H I 9–6
5.9156	5.9165	0.019 ± 0.005	He II 22–13
5.9533	5.9533	0.027 ± 0.003	He II 28–14
5.9559	5.9568	0.163 ± 0.021	H I 14–7
5.9636	5.9646	0.181 ± 0.016	He II 15–11
5.9812	5.9820	1.732 ± 0.020	[K IV]
6.0540	6.0549	0.010 ± 0.002	H I 42–8
6.0652	6.0662	0.005 ± 0.001	H I 41–8
6.0780	6.0784	0.005 ± 0.001	H I 40–8
6.0908	6.0916	0.007 ± 0.002	H I 39–8
6.1076	6.1086	0.363 ± 0.007	H_2 0–0 S(6)
6.1500	6.154	0.206 ± 0.017	[Ca VII]
6.2233	6.2243	0.016 ± 0.002	H I 32–8
6.2420	6.2431	0.044 ± 0.010	He II 21–13
6.2506	6.2516	0.018 ± 0.002	H I 31–8
6.2882	6.2894	0.042 ± 0.005	He II 26–14
6.2909	6.2919	0.241 ± 0.015	H I 13–7
6.3796	6.3816	0.097 ± 0.017	[Zn VII]
6.3956	6.3969	0.017 ± 0.006	H I 27–8
6.4444	6.4455	0.011 ± 0.003	H I 26–8
6.4932	6.4923	3.610 ± 0.389	[Si VII] + [Ni VII]?
6.5380	6.5394	0.095 ± 0.012	He II 17–12
6.5636	6.5647	0.021 ± 0.005	H I 24–8
6.6347	6.6359	0.036 ± 0.004	[Ni II]
6.6373	6.6384	0.019 ± 0.002	H I 23–8
6.6664	6.6677	0.038 ± 0.004	He II 20–13
6.7056	6.7067	3.107 ± 0.077	[Cl V]
6.7212	6.7213	0.014 ± 0.002	[Fe II]
6.7232	6.7245	0.067 ± 0.007	H I 22–8 + [Zn VI]
6.7682	6.7692	0.046 ± 0.014	He II 24–14
6.7710	6.7720	0.326 ± 0.014	H I 12–7

Table 2 – *continued*

λ_{obs} (μm)	λ_{rest} (μm)	Flux	Species
6.8248	6.8259	0.031 ± 0.007	H I 21–8
6.9080	6.9095	2.108 ± 0.052	H_2 0–0 S(5)
6.9472	6.9480	1.956 ± 0.070	He II 9–8
6.9844	6.9853	Saturated	[Ar II]
7.0920	7.0927	0.070 ± 0.005	H I 19–8
7.2040	7.2048	0.234 ± 0.006	He II 14–11
7.2392	7.2400	0.045 ± 0.002	He II 19–13
7.2704	7.2717	0.027 ± 0.002	H I 18–8
7.3168	7.3178	9.117 ± 0.410	[Na III]
7.4554	7.4568	0.909 ± 0.10	He II 12–10
7.4588	7.4599	6.050 ± 0.405	H I 6–5
7.4696	7.4738	0.844 ± 0.025	[Mn VII]
7.4941	7.4951	0.091 ± 0.010	H I 17–8
7.4981	7.4994	0.288 ± 0.030	He II 16–12
7.5014	7.5025	1.712 ± 0.105	H I 8–6
7.5070	7.5081	0.436 ± 0.058	H I 11–7
7.6550	7.6524	Saturated	[Ne VI]
7.7797	7.7804	0.067 ± 0.013	H I 16–8
7.8123	7.8141	0.399 ± 0.048	[Fe VII]
7.9007	7.9016	35.280 ± 0.395	[Ar V]
8.0098	8.0103	0.024 ± 0.005	He II 25–15
8.0241	8.0250	1.108 ± 0.012	H_2 0–0 S(4)
8.0372	8.0385	0.030 ± 0.009	He II 21–14
8.0476	8.0490	0.072 ± 0.009	He II 18–13
8.1508	8.1549	0.016 ± 0.002	He II 30–16
8.1540	8.1549	0.101 ± 0.003	H I 15–8
8.1711	8.1724	0.010 ± 0.002	H I 29–9
8.2352	8.2362	0.018 ± 0.002	H I 28–9
8.3076	8.3084	0.010 ± 0.003	H I 27–9
8.4118	8.4128	0.018 ± 0.006	He II 24–15
8.4831	8.4849	0.012 ± 0.002	H I 25–9
8.6079	8.6106	20.001 ± 1.682	[Na VI]
8.6595	9.6610	0.031 ± 0.004	He II 28–16
8.6632	8.6645	0.085 ± 0.009	H I 14–8
8.7184	8.7206	0.029 ± 0.006	H I 23–9
8.7557	8.7565	0.082 ± 0.009	He II 20–14
8.7591	8.7601	0.384 ± 0.062	H I 10–7
8.8289	8.8299	0.853 ± 0.111	[K VI]
8.8684	8.8697	0.015 ± 0.002	H I 22–9
8.9190	8.9209	0.017 ± 0.003	He II 23–15
8.9892	8.9914	Saturated	[Ar III] + [Mg VII]
9.0399	9.0410	3.541 ± 0.160	[Na IV] + H I 21–9
9.1126	9.1158	0.085 ± 0.004	[Al VI] + He II 15–12
9.1321	9.1353	0.022 ± 0.003	[Fe II]
9.2596	9.2605	0.017 ± 0.002	H I 20–9
9.2725	9.2736	0.042 ± 0.004	He II 17–13
9.3868	9.3882	0.017 ± 0.002	He II 26–16
9.3907	9.3920	0.088 ± 0.011	H I 13–8
9.5234	9.5261	0.697 ± 0.075	[Fe VII]
9.6638	9.6649	2.065 ± 0.050	H_2 0–0 S(3)
9.7055	9.7068	0.160 ± 0.012	He II 13–11
9.7122	9.7135	0.599 ± 0.011	He II 10–9
9.7691	9.7707	0.028 ± 0.001	He II 19–14
9.8455	9.8470	0.007 ± 0.001	H I 18–9
9.8784	9.8796	0.008 ± 0.001	He II 25–16
9.8784	9.88		[Ni VIII] + [Zn VII]
10.2597	10.2613	0.023 ± 0.003	H I 17–9
10.5085	10.5105	Saturated	[S IV]
10.6425	10.6440	0.036 ± 0.002	[Cr VI]
10.8019	10.8036	0.031 ± 0.004	H I 16–9
10.8443	10.8459	0.033 ± 0.004	[Mn VI]
10.8524	10.8543	0.006 ± 0.001	H I 25–10

Table 2 – *continued*

λ_{obs} (μm)	λ_{rest} (μm)	Flux	Species
10.8804	10.88	0.019 ± 0.002	[Co VII]
11.3019	11.3041	0.087 ± 0.012	He II 18–14
11.3070	11.3087	0.548 ± 0.012	H I 9–7 + [Ni I]?
11.3315	11.3334	0.283 ± 0.020	[Cl I]
11.4823	11.4824	0.042 ± 0.005	[Ca V]
11.4896	11.4920	0.021 ± 0.003	H I 22–10
11.5381	11.5395	0.037 ± 0.004	H I 15–9
11.7612	11.7590	1.385 ± 0.026	[Cl IV]
12.1562	12.1568	0.017 ± 0.004	H I 20–10
12.2470	12.2485	0.012 ± 0.004	He II 25–17
12.2762	12.2786	0.939 ± 0.021	H_2 0–0 S(2)
12.3038	12.3107	0.039 ± 0.004	[Fe VI]
12.3651	12.3668	0.345 ± 0.024	He II 14–12
12.3703	12.3719	1.962 ± 0.024	H I 7–6
12.3856	12.3872	0.235 ± 0.016	H I 11–8
12.5863	12.5871	0.091 ± 0.008	H I 14–9
12.6088	12.6110	0.016 ± 0.003	H I 19–10
12.8125	12.8135	Saturated	[Ne II]
13.1012	13.1022	Saturated	[Ar V]
13.1263	13.1283	0.543 ± 0.015	He II 11–10
13.1862	13.1880	0.017 ± 0.004	H I 18–10
13.2137	13.2155	0.006 ± 0.001	He II 24–17
13.3813	13.40	0.153 ± 0.020	[F V]?
13.5188	13.5210	5.741 ± 0.118	[Mg V]
13.6062	13.6080	0.028 ± 0.006	He II 19–15
13.8737	13.8776	0.037 ± 0.002	He II 17–14
13.9012	13.9044	0.012 ± 0.002	He II 21–16
13.9388	13.9418	0.026 ± 0.007	H I 17–10
14.1750	14.1773	0.023 ± 0.003	He II 26–18
14.1804	14.1831	0.112 ± 0.013	H I 13–9
14.3213	14.3217	Saturated	[Ne V]
14.3638	14.3678	1.631 ± 0.158	[Cl II]
14.3938	14.3964	Saturated	[Na VI]
14.7078	14.7098	0.023 ± 0.006	H I 22–11
14.7788	14.7710	0.119 ± 0.014	[Fe VI]
14.9587	14.9623	0.022 ± 0.006	H I 16–10
15.3912	15.3960	0.105 ± 0.031	[K IV]
15.4712	15.4713	0.097 ± 0.018	He II 15–13
16.2011	16.2025	0.085 ± 0.018	He II 20–16
16.2073	16.2091	0.325 ± 0.012	H I 10–8
16.4088	16.4117	0.033 ± 0.007	H I 15–10
16.8787	16.8806	0.145 ± 0.020	H I 12–9
17.0312	17.0348	1.201 ± 0.023	H_2 0–0 S(1)
17.2588	17.2609	0.272 ± 0.015	He II 12–11
17.8838	17.8846	0.070 ± 0.020	[P III]
17.9338	17.9360	0.241 ± 0.016	[Fe II]
17.9825	17.9860	0.332 ± 0.092	[Ca VI]
18.7110	18.7130	49.025 ± 0.366	[S III]
19.0590	19.0619	0.706 ± 0.037	H I 8–7
19.5510	19.5580	0.144 ± 0.031	[Fe VI]
20.3070	20.3107	0.597 ± 0.078	[Cl IV]
21.2570	21.29	0.352 ± 0.111	[Na IV]
21.8270	21.8291	1.956 ± 0.074	[Ar III]
24.3170	24.3175	273.000 ± 3.424	[Ne V]
25.2430	25.2490	0.327 ± 0.091	[S I]
25.8850	25.8903	222.100 ± 3.697	[O IV]
25.8970	25.8999	31.830 ± 3.697	He II 23–19
25.9810	25.9884	0.896 ± 0.078	[Fe II]

Note. [Mg VII] at 5.50 μm is saturated at the line centre, but detected at side lobes.

9.88 μm [Ni VIII] + [Zn VII] line is too weak to measure the intensity.

Table 3. Ionization potentials (IPs) of species observed in the integrated MRS spectrum of NGC 6302. The listed IPs are those of the next lowest ion, i.e. the photon energy needed to form the detected ion (collisionally excited lines) or the recombining ion (permitted lines).

Species	IP (eV)	Species	IP (eV)	Species	IP (eV)
H I	13.6	[P III]	19.8	[Cr VI]	69.5
He II	54.4	[S I]	0.0	[Cr IX]	184.8
[O IV]	54.9	[S III]	23.3	[Mn VI]	72.4
[F V]	87.2	[S IV]	34.8	[Mn VII]	95.6
[Ne II]	21.6	[Cl I]	0.0	[Fe II]	7.9
[Ne III]	41.0	[Cl II]	13.0	[Fe VI]	75.0
[Ne V]	97.1	[Cl IV]	39.6	[Fe VII]	99.1
[Ne VI]	126.2	[Cl V]	53.5	[Fe VIII]	125.0
[Na III]	47.3	[Ar II]	15.8	[Co VII]	102.0
[Na IV]	71.6	[Ar III]	27.6	[Ni I]	0.0
[Na VI]	138.4	[Ar V]	59.8	[Ni II]	7.6
[Mg V]	109.3	[K V]	45.8	[Ni VIII]	132.7
[Mg VII]	186.8	[K VI]	82.7	[Zn VI]	82.6
[Al VI]	153.8	[Ca V]	67.3	[Zn VII]	108.0
[Si VII]	205.3	[Ca VII]	108.8		

4.1.2 PAHs

The abundance analysis of NGC 6302's ionized lines shows that the nebula is oxygen-rich (C/O $\sim$ 0.4; Wright et al. 2011). It is known that NGC 6302 exhibits bands from carbonaceous PAH molecules (Roche & Aitken 1986; Molster et al. 2001; Cohen & Barlow 2005), despite being oxygen-rich.

The integrated spectrum shows clear features from PAH molecules. These are visible at 5.85–6.5 μm, 11.2 μm, and a weak band at 12.0 μm is present. Additional features are expected at 7.7 and 8.6 μm, but these spectral regions are affected by artefacts from the very strong atomic emission lines at these wavelengths, which makes it difficult to confidently identify the features. A potential 12.7 μm feature coincides with the saturated [Ne II] 12.81 μm emission line and thus the presence or absence of the PAH feature cannot be determined.

4.1.3 Dust features

NGC 6302 was already known to exhibit strong crystalline silicate features (e.g. Molster et al. 1999, 2001; Kemper et al. 2002). Most of these features are found at wavelengths longer than 18 μm (Fig. 2). Forsterite dominates most of the features (Molster, Waters & Tielens 2002; Chihara, Koike & Tsuchiyama 2007), but the presence of some enstatite features at 17–25 μm has been suggested (Hofmeister & Bowey 2006). These features are detected and are labelled in Fig. 2.

The dust features have been compared with dust mass absorption coefficients in order to make their identifications. When dust optical constants are provided, the dust mass absorption coefficients are calculated by the continuous distribution of spheroids (Min, Hovenier & Koter 2003). Optical constants and dust mass absorption coefficients are taken from Suto et al. (2006), Koike et al. (2010), and Zeidler et al. (2011) (forsterite), Murata et al. (2009) and Zeidler, Mutschke & Posch (2015) (enstatite), and Zeidler, Posch & Mutschke (2013) (quartz). Approximately 5 per cent of the dust mass is composed of crystalline silicates with forsterite and quartz dominating (see Appendix B), as opposed to amorphous silicates.

In addition to these known crystalline silicate features, the high-quality MIRI spectra reveal additional features. Using the optical constants taken from Zeidler et al. (2013), the feature at 25 μm is likely due to quartz (SiO_2). Quartz should also have broad features at 18 and 21 μm; however, these features are blended with the forsterite and enstatite features.

We also compared with the dust mass absorption coefficients of Ca-containing pyroxene (Koike et al. 2000), olivine (Zeidler et al. 2015), and fayalite (Fabian et al. 2001); however, it seems that these constituents are not major contributors to the observed dust emission spectrum.

4.2 Line maps

Once the lines are identified from the integrated spectra, the next stage is to build spectral maps. Extraction of line images from the data cubes requires subtracting the continuum. For each line, a number of wavelength pixels (4 pixels by default) were selected to cover the emission line. If the adjacent continuum contained no other lines or features, the continuum level was taken as the average of segments consisting of the same number of wavelength pixels on the short and long wavelength sides of the line. The pixel-by-pixel mean of these two images was subtracted from the channel images. The line images were converted from units of surface brightness (MJy sr^{-1}) to line flux (W m^{-2} pixel^{-1}) using the wavelength spacing between the channels, and these individual line flux images were summed to make an output line flux image. A set of representative line maps is presented in Fig. 3.

In some cases, the continuum regions could not be selected immediately adjacent to the spectral line of interest. In these instances, either continuum regions slightly further from the line of interest were used or the continuum level was taken from only one side of the line. At the shorter wavelengths, where more lines are present, the continuum slope is usually small over the wavelength range around a line where the continuum regions are defined, and using a one-sided continuum estimation does not appear to introduce much of a residual continuum in the line image.

In some instances, for very weak lines, the attempt to make a line image failed because the line signal was of the same magnitude as the uncertainties or noise in the continuum image, but for many lines the output line images clearly trace a different morphology than the continuum at that wavelength. For some of the saturated lines, some limited line image information can be obtained from the short-wavelength or long-wavelength wing of the line.

4.3 The central source

The nature of the photoionizing source at the heart of NGC 6302 has long been uncertain due to its concealment by abundant dust towards the centre. Previous mid-IR observations lacked the spatial resolution to confirm its location and sensitivity, while an apparent optical detection in *HST* images turned out to be a serendipitous alignment of a foreground star with the approximate geometric centre of the nebula (Szyszka et al. 2009; Kastner et al. 2022).

Now, on the other hand, our *JWST* observations clearly reveal a bright, compact IR source at the heart of the nebula, at RA = 17:13:44.488 $\pm$ 0.004, Dec. = −37:06:11.76 $\pm$ 0.03. This confirms the tentative identification of the central source at this location in *L*-band imaging by Matsuura et al. (2005). No corresponding source is detected at this position at optical wavelengths. The nature of the central source will be discussed by Wesson et al. (in preparation).

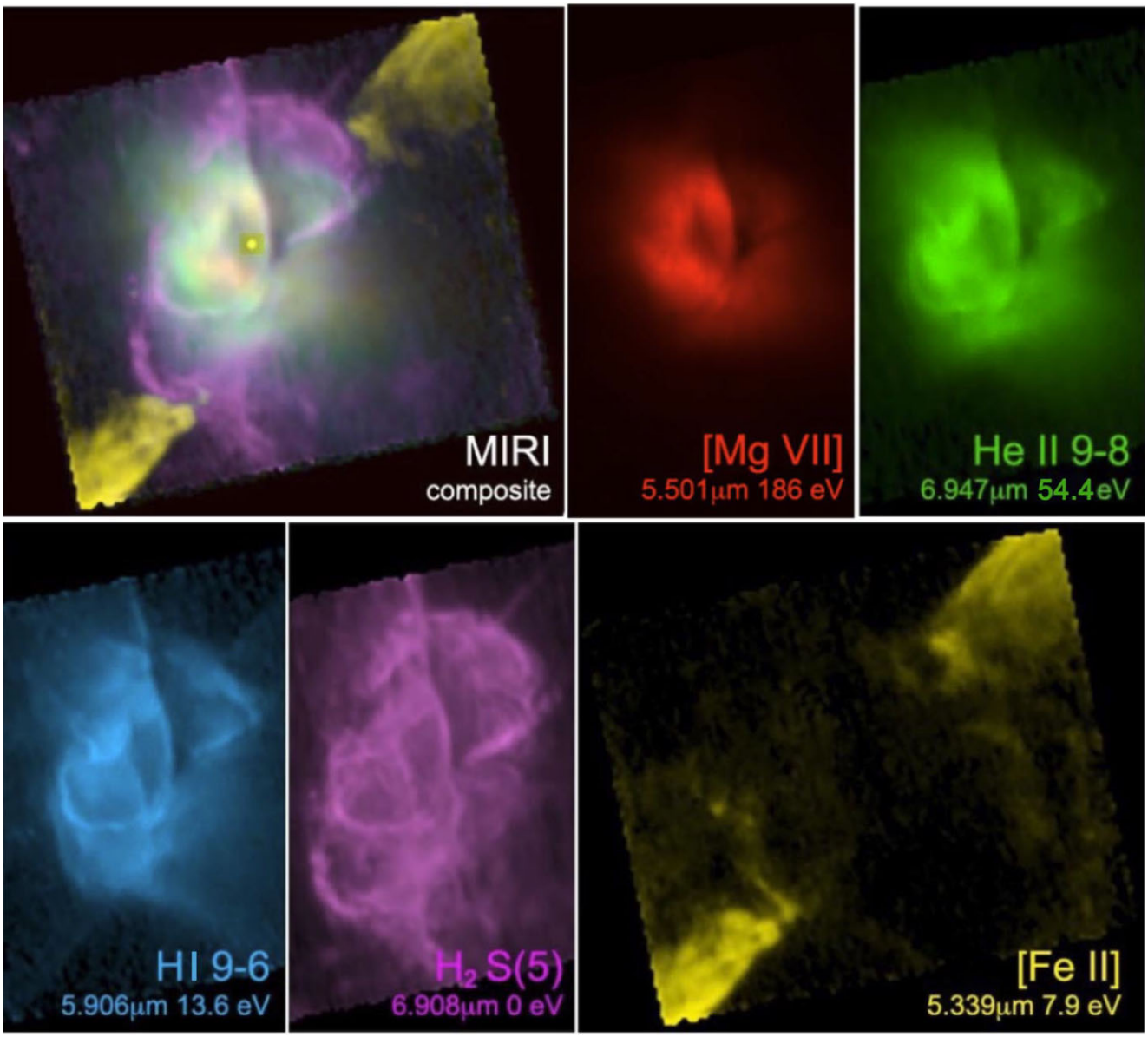

Figure 3. Five-colour composite image of NGC 6302, for lines from a range of ionization potentials with 5.50 μm [Mg VII] (186 eV), the second-highest ionization potential line, to molecular H_2. Each line indicates the ionization energy of the parent species.

4.4 Morphology

Fig. 3 shows representative line maps, demonstrating the strength of MIRI's IFU capability. In this figure, different colours are allocated to different lines. The MIRI composite image (top left) shows the trend of increasing spatial extent of the emission, when going from highly ionized species such as [Mg VII] to lower ionization tracers, culminating in the H_2 line. This is well traced by different colours, with [Mg VII] being the most compact, and H I and H_2 the most extended.

The central region shows clear ionization stratification. [Mg VII], the second-highest ionization emission (186.8 eV), forms a relatively smooth, compact ring. The ring is partly bisected by a vertical dark band, caused by extinction from the torus, as illustrated in Fig. 4. There is a hole inside the ring. The emission running from the north to south on the hole is due to the emission from the surface of the nearly edge-on torus.

The He II image, which arises from recombining He^{++} atoms, is centred similarly to [Mg VII] but lacks the clear circular ring structure, and instead appears elongated. The emitting region is larger and shows a well-defined edge along a position angle of approximately 20° west of a north–south axis. Further out than He II, the H I recombination lines, which trace H^+, show an elongated structure with a much clearer edge and arcs. Exterior to that the H_2 image shows a second, larger arc at a position angle of approximately 20° of the north–south line.

A schematic picture of the central region of NGC 6302 is presented in Fig. 4. A torus runs north–south, which is detected in the ^{13}CO 2–1 rotational line (see also Fig. 1) and partly in the dust extinction (Section 4.6). The torus appears distorted or warped (Icke 2003) at the outermost regions.

The nebula shows a series of H^+ arcs, seen in the H I recombination line image. Some of these delineate two lobes with clear edges in

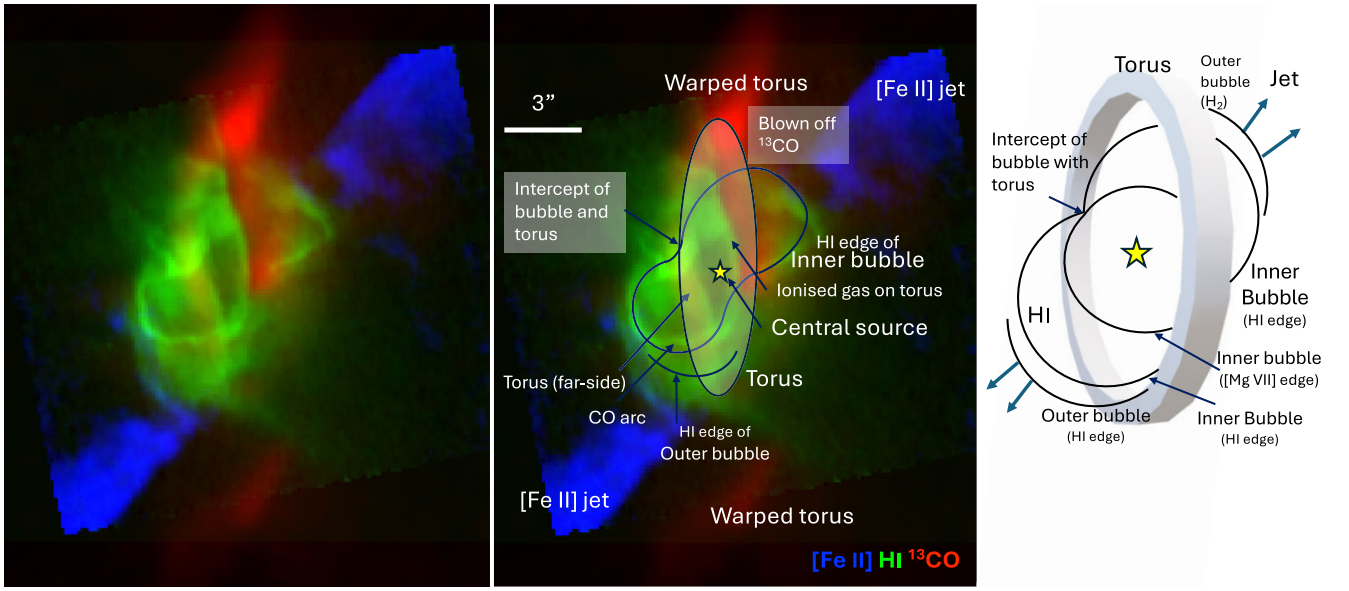

Figure 4. Three-colour composite image of NGC 6302: 5.91 μm H I 9–6 (green), 5.34 μm [Fe II] (blue), and ALMA ^{13}CO J = 2–1 (red). Several components, such as a warped torus, inner and outer bubbles, and [Fe II] jets are labelled. The ‘CO arc’ refers to a short segment of the arc that is visible in ^{13}CO (left panel; also in Fig. 7), and is part of the inner bubble. The north part of the outer bubble is found only in H_2, which is shown in Figs 1 and 7.

Fig. 4. We consider the two brighter arcs oriented south-east and north-west to be a single structure, which we will call the ‘inner bubble’. It appears to be broken into two parts due to dust extinction across the torus. The inner bubble is peanut-shaped. The pinched waist of the peanut shape occurs where the bubble intercepts the torus. Elsewhere, it interacts with less dense material and has expanded further (Section 4.5.1). There is a further H^+ rim exterior to the inner bubble, which we will call the ‘outer bubble’.

4.4.1 [Fe II] and [Ni II] jets

The [Fe II] image reveals two jets extending in nearly opposite directions, with position angles of approximately −35° and +145° (Fig. 3). These jets were previously detected in *HST* images (Kastner et al. 2022; Balick et al. 2023). However, for the first time, *JWST*’s MIRI MRS has provided velocity-resolved observations of these jets, achieving a spectral resolution of $\Delta v \sim 45$ km s^{-1} at 5 μm, and potentially even better than <40 km s^{-1} (Jones et al. 2023). The jets exhibit velocity spreads ranging from approximately −115 to +110 km s^{-1} in the rest frame (Fig. 5).

All six [Fe II] lines, along with a [Ni II] line (Fig. 6) detected in the MIRI spectra, display jets with consistent morphology and velocity expansion.

The [Fe II] jets originate outside the H_2 emission region, or outer bubble, but do not exhibit a jet structure interior to the outer bubble (Fig. 4). At the outer bubble, there is an arc-like rim that is prominent in H_2. The bases of the pair of large [Fe II] ‘plumes’ connect to this arc where it meets the edges of the butterfly wing (Fig. 4).

Although the jets appear to be point symmetric, their centre of symmetry does not align with the central star but is instead offset to the south.

In addition to the two point-symmetric jets, faint [Fe II] emission is detected throughout the outflow. This includes emission along the H^+ rim of the inner bubble, at the intercept, and within the interiors of both the eastern and western bipolar outflows.

The velocity map in Fig. 5 represents the rest-frame velocity with respect to the local standard of rest (LSR). The Doppler shift of the gas was measured using MIRI wavelengths in the solar system barycentric frame and then converted to $v_{\rm LSR}$. The systemic radial velocity of NGC 6302 (−30 km s^{-1} in $v_{\rm LSR}$; Santander-García et al. 2016) was subsequently subtracted. The rest-frame wavelength of the [Fe II] line at 5.3401693 μm is adopted from the NIST data base.[6]

4.5 Stratification: from ionized lines to H_2 and PAHs

The MIRI IFU data enable us to detect and obtain maps of over 100 lines from neutral atoms and ions with a large range of ionization potentials: from 7.6 eV to above 200 eV. Fig. 3 demonstrates the stratification of several of these lines. Fig. 6 includes more atomic lines with slightly different ionization potential energies. In general, lines from high ionization-potential species tend to be compact, whereas lines from lower ionization-potential species trace more extended gas. Several arc-like filaments are embedded in the more extended gas, as seen in Figs 6 and 7. Fig. 7 includes ^{13}CO, which traces the torus, showing the relative positions of ionized gas to the torus. Fig. 7 also demonstrates the distributions of H_2 and PAH emission.

4.5.1 The inner bubble and its stratification

Clear stratification is observed inside (labelled in Fig. 7): the physical implications of the bubble will be discussed in Section 5.3. For example, lines from high-ionization species, such as the [Si VII] 6.49 μm line (Fig. 6), show low intensity interior to this rim, and instead is concentrated in a more compact shell.

The line that traces ions of the second-highest ionization potential (185 eV) is [Mg VII]. The Mg[6] gas is also situated in a compact shell close to the centre (Fig. 3). On the other hand, the He II and H I

[6]https://www.nist.gov/pml/atomic-spectra-database

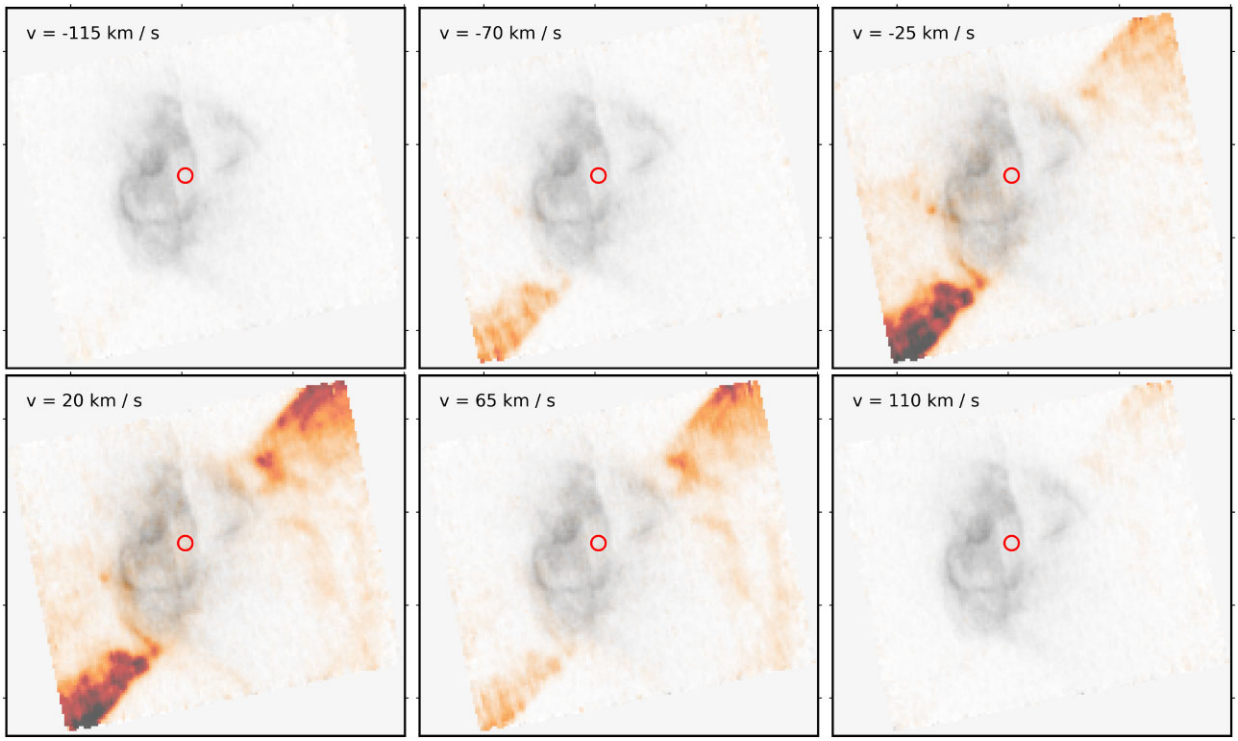

Figure 5. The MIRI channel map of the 5.3 μm [Fe II] jet is shown. The jet, highlighted in red, extends from the south-east and the north-west edges of the outer bubble. The south-eastern part of the jet is blueshifted, while the north-western part is redshifted. The velocity labels represent rest-frame velocities in the LSR, obtained by subtracting the radial velocity of NGC 6302 from the velocities measured with MIRI. For positional reference, the integrated image of the 5.13 μm H I 10–6 line is plotted in grey. The red circle shows the position of the central source. The orientation is north at the top, and east to the left. The declination grid is marked at intervals of 5 arcsec. Video version of the jet is available online.

line emission is relatively weaker at the Mg^6 gas emitting region, and is stronger further out. The H I emission is strongest in filaments, broken in places. Such a stratification was previously suggested from long-slit spectra of four atomic lines at 2–4 μm (Casassus, Roche & Barlow 2000), but is more clearly evident and spatially identified by MIRI.

An exception to the stratification is where the inner bubble 'intercepts' the torus (Fig. 7). At the intercepts, [Mg VII], He II, and H I lines are all present as demonstrated in Fig. 3. This intercept is the brightest point in the H I line image.

4.5.2 *Stratification of H^+, H_2, and PAHs at the inner bubble*

Stratification is also found among H^+ and H_2 lines and PAHs at the rim of the inner bubble and its exterior. Fig. 7 shows (a) the three-colour composite image of H I, H_2, and PAH emission and (b) the H I, PAHs, and ^{13}CO image. The ^{13}CO image is used to indicate the location of the molecular torus. Fig. 7(b) is enlarged on the right top panel to see the detailed structures at the bubble and the torus. The H^+ gas is traced by the emission of 5.91 μm H I 9–6 line. The PAH image is a continuum-subtracted image taken at 6.3 μm, where the 'continuum' (presumed to be mainly silicate emission) was estimated from 6.0 and 6.5 μm, which accounts for about 30 per cent of the total intensity. The H_2 image is from the S(5) line at 6.910 μm.

Fig. 7(a) shows that H I and H_2 are emitted from the same location at the inner bubble (within the MIRI spatial resolution), as the bubble appears as pink in this H I (blue) and H_2 (red) overlay. In contrast, PAHs are found slightly outwards from H I, as shown in Fig. 7(b) and (b) enlarged.

In the outer bubble, PAH emission overlaps with that of H_2, or the H_2 emission is found outside the PAH emission. This indicates a difference between the stratification of the inner bubble and the larger outer bubble.

The order of the stratification of H^+, H_2, and PAHs at the inner bubble of NGC 6302 looks different from a typical PDR stratification. In Orion Bar, the PAH emission appears immediately behind (3×10^{-3} pc) the H^+, ionization front, and the H_2 ridge appears further away by 0.02 pc (Habart et al. 2024).

4.5.3 *Stratification in the torus*

Panel (b) enlargement in Fig. 7 illustrates the stratification of ^{13}CO, H^+, and PAHs in the far-side torus. The ^{13}CO emission appears as a long, near-vertical filament along the centre of the torus. PAH emission is present on both sides of the ^{13}CO structure. The H I and H_2 emissions are located alongside ^{13}CO with a slight offset to the east (Figs 7a and enlarged panel b), whereas on the west side they overlap with ^{13}CO. Additionally, both H^+ and H_2 exhibit more extended emission on the east side (Figs 7c and e).

4.6 Dust extinction

4.6.1 *Extinction map*

The images show a prominent dark lane seen in extinction, running from the north to south, over the full wavelength range covered by the MIRI IFU and *HST* (Figs 1 and 3). This dark lane is attributed to the torus, also seen in ^{13}CO ALMA emission (Fig. 1). There

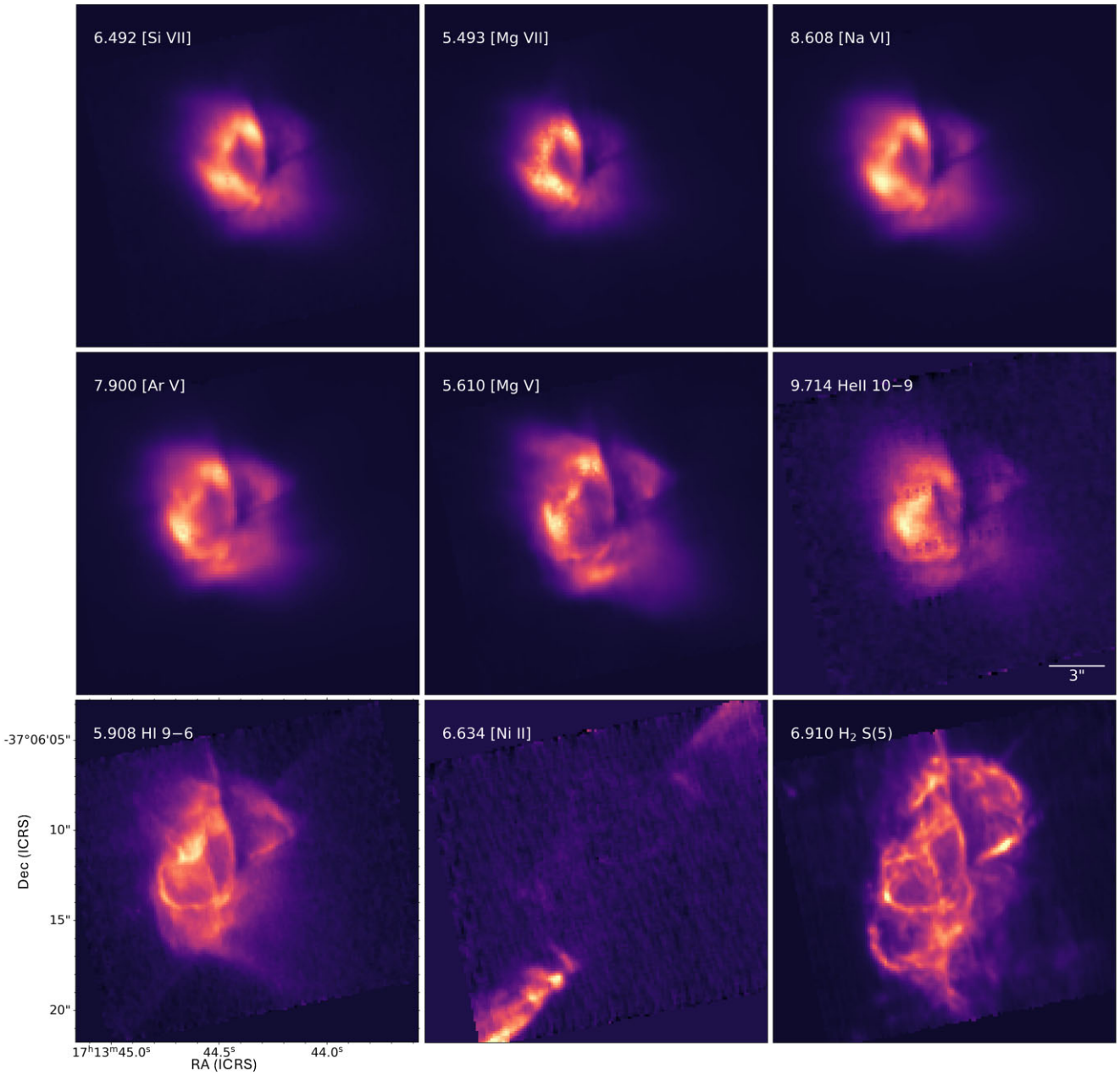

Figure 6. NGC 6302 integrated line maps. From the left top [Si VII] to the right column [Na VI] and then to the middle bottom [Ni II] the atomic line maps are placed in order of a higher ionization line to a lower ionization line, followed by an H_2 molecular image. Higher ionization lines are more compact than lower ionization lines, and H_2 is much more extended, with many filaments within. [Ni II] and [Fe II] (Fig. 3) show jet structures. In H_2, there is a secondary arc outside of the inner bubble in the south-east tip. This corresponds to the outer bubble. North is towards the top, and east is to the left. Square dots in the 9.714 μm He II image are artefacts usually resulting from an outlier detection on a residual warm pixel.

is significant dust extinction from this torus of the nebula, out to wavelengths as long as 25 μm. This extinction far exceeds the foreground ISM extinction to NGC 6302, $A(V) = 1.6$ mag from $E(B-V) = 0.53$ mag (Section 2.1).

To obtain the total optical depth at the reference wavelength of 5.91 μm at the H I 9–6 line, the ALMA observation of NGC 6302 in the millimetre recombination line H30 α was compared to the MIRI line flux. The extinction at 1292.7609 μm (231.90093 GHz) H30 α line is assumed to be negligible. The ratio image H30 α/H I 9–6 has the largest value in the dark lane because of the reduction of the H I 9–6 line intensity. The intrinsic line ratio of H30 α/H I 9–6 is calculated from case B, where all the lines, apart from the Lyman lines, are optically thin (Hummer & Storey 1987). A large grid of CLOUDY version 23.01 (Chatzikos et al. 2023) case B models was calculated covering the hydrogen density range from 10^2 to 10^6 cm^{-3} and temperatures between 5000 and 15 000 K. The case B ratio shows the most variation for lower densities, which are not applicable for NGC 6302. For densities at or above 80 000 cm^{-3}, the typical density value from the MOCASSIN model of the nebula from Wright et al. (2011), the range of the value of the line ratio is restricted to between about 0.00012 and 0.00016. We used the minimum of this range to avoid having ratio values lower than the

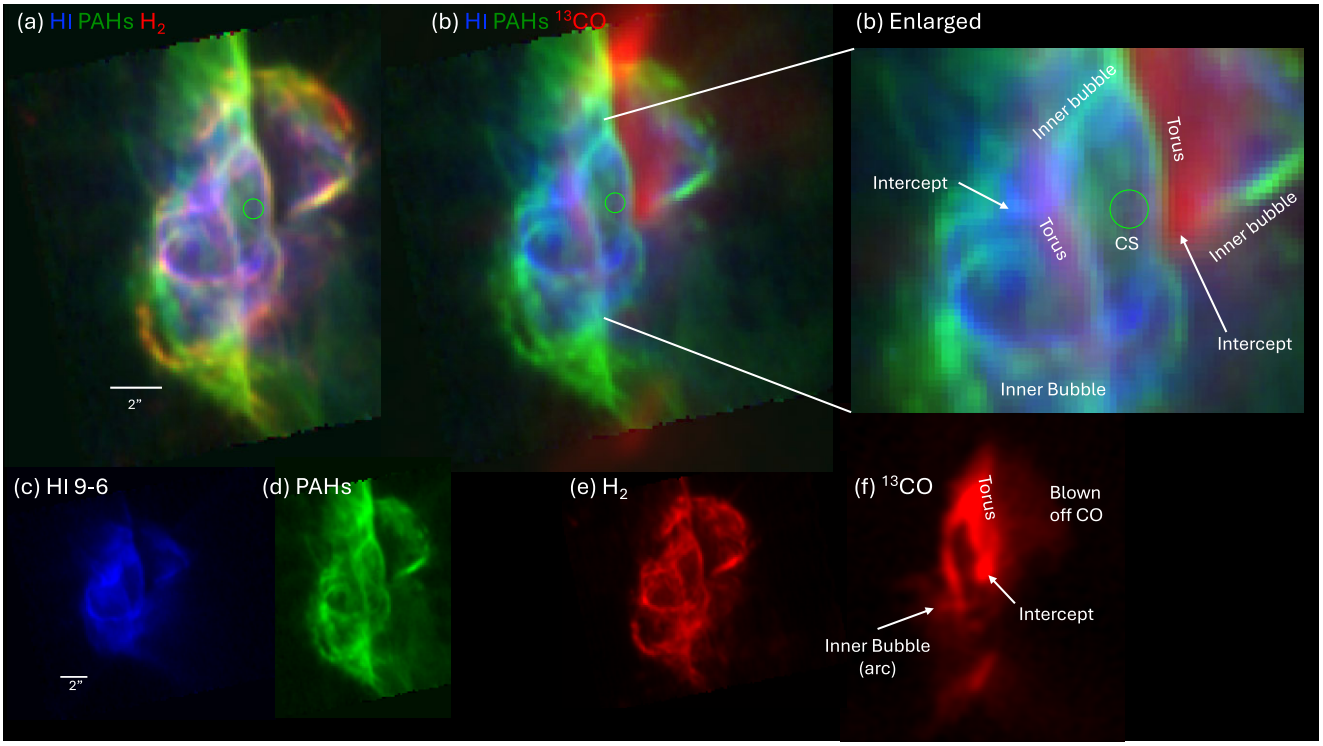

Figure 7. Stratification of H^+, PAHs, and H_2, with a ^{13}CO image displaying the torus. With MIRI's angular resolution, H^+ and H_2 mostly overlap at the bubble (a), as found in pink colour, while PAH emission is found outside of H^+ at the bubble (b enlarged). On the other side, on the outside of the bubble, PAHs are found inside of H_2. ^{13}CO traces the molecular torus: its front and rear sides, and the outer extended (warped) regions. Additionally, ^{13}CO emission is found at a part of the inner bubble (arc). In the enlarged image (b), stratification of ^{13}CO, H^+, and PAHs is found. The green circle indicates the location of the central source (CS). The H^+ gas is traced by the emission of 5.91 μm H I 9–6 line, while PAHs is from 6.3 μm band, and H_2 is traced by 6.91 μm H_2 0–0 S(5) line.

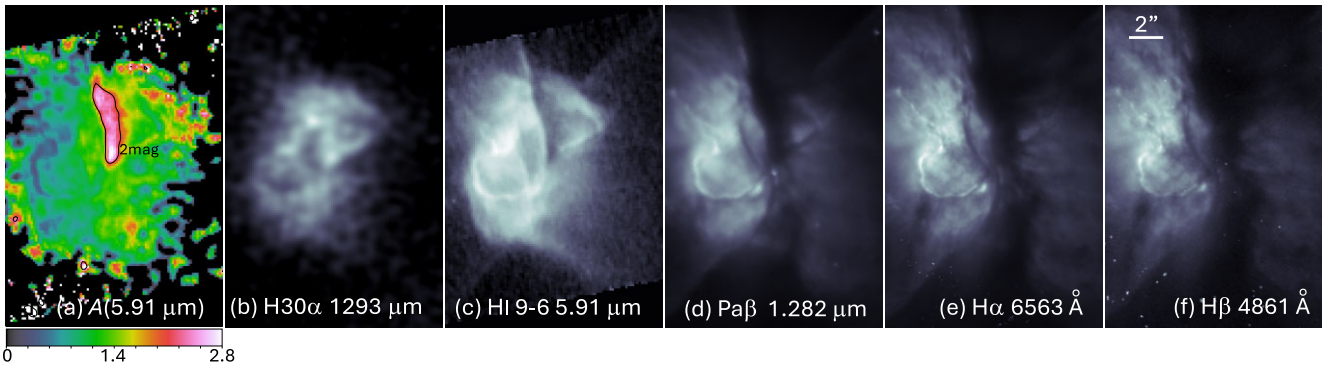

Figure 8. (a) The relative extinction in magnitudes across the nebula at the H I 9–6 line (5.91 μm). The black contour line traces with $A(5.91\,\mu m) = 2$ mag, the highly extinguished region by the torus foreground to the bipolar outflow. The relative extinction is derived from the comparison of the images of (b) the ALMA H30α line flux to (c) the H I 9–6 line flux with respect to the minimum value of case B from CLOUDY models. The *HST* (d) Paβ, (e) Hα, and (f) Hβ (Kastner et al. 2022) are plotted in comparison, showing the decrease of extinction with longer wavelength in the torus. The north-west edge of the inner bubble, which serves as the background to the bipolar outflow, is visible only at IR wavelengths (Fig. 4).

case B prediction within the bright part of the nebula in the MIRI images.

To make the extinction map (Fig. 8), the case B minimum value of 0.00012 was used as the unextinguished reference ratio for calculating extinction values across the nebula. Consequently, the extinction values so derived represent the maximum possible extinction because the minimum case B ratio was used as a comparison. If the larger ratio value of 0.000179 from the full CLOUDY model is used instead, the total extinction at 5.91 μm in the middle of the dark dust lane at RA = $17^h13^m44\overset{s}{.}40$ and Dec. = $-37°06'10\overset{''}{.}63$ drops from 2.36 to 1.92 mag. So, the extinction uncertainty ranges down 0.4 mag from the values shown in Fig. 8 for the high extinction areas of the map, although it seems likely that the actual unextinguished reference value to use for the calculation will be somewhere between the full model value and the case B minimum value given the range of ratio values seen from the image comparison.

The extinction curve used here predicts an extinction of about 0.042 mag at 5.907 μm from the foreground reddening of

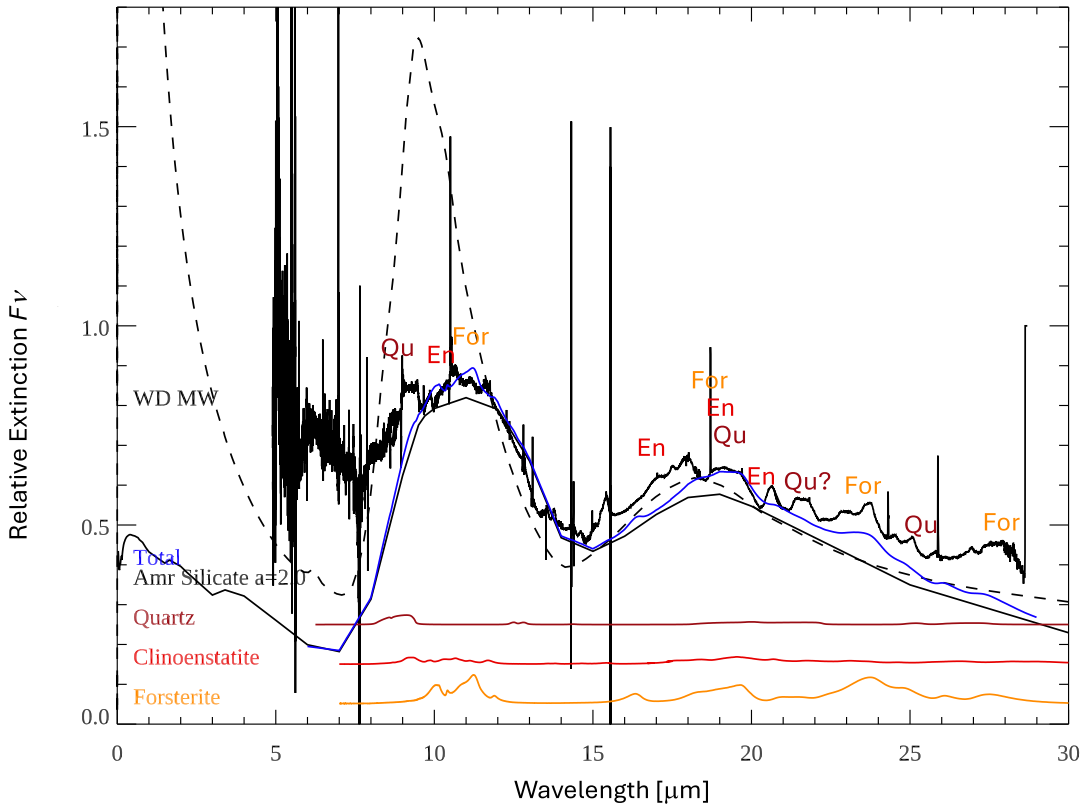

Figure 9. The derived relative extinction values as a function of wavelength at the torus. The dust mass absorption coefficients κ for the Milky Way ISM (WD MW; Weingartner & Draine 2001), amorphous silicate with 2 μm grain size (Draine & Lee 1984), crystalline silicates, Quartz (Qu; Zeidler et al. 2013), Enstatite (En; Murata et al. 2009), and Forsterite (For; Koike et al. 2010) are also plotted. Major features are labelled.

$E(B-V) = 0.53$ mag. This is much smaller than the extinction measured in Fig. 8. Hence, the large majority of the extinction originates inside NGC 6302.

4.6.2 *Wavelength dependence of the extinction*

Extinction can be measured by the reddening induced by the wavelength dependence of the dust absorption and scattering (e.g. Rieke & Lebofsky 1985). One method is by using the observed relative line intensities of hydrogen or helium recombination lines. There are several such lines detected in the MIRI data, such as the hydrogen recombination lines H I 10–6 (5.13 μm), H I 9–6 (5.91 μm), H I 10–7 (8.76 μm), and H I 8–7 (19.06 μm). However, dust extinction curves in the mid-IR show a complex wavelength dependence caused by various silicate bands (Section 4.1.3), which can vary from typical ISM environments (e.g. Weingartner & Draine 2001). This makes this method difficult to apply. Indeed, the observed ratios of the mentioned lines, compared to predictions from a large grid of case B recombination line calculations from the CLOUDY code (version 23.01; Chatzikos et al. 2023) using standard extinction curves, did not give consistent results.

Instead, we determine the wavelength dependence of the extinction component from the torus directly from the spectral profiles of the MIRI IFU slices. A cut across the absorption band was selected from the channel 1-short IFU slices, along Dec. $= -37°06'10\overset{''}{.}63$. We assume that the emitted flux varies smoothly across the absorption band and can be approximated via a linear interpolation across the absorption feature. An interpolation was carried out from peak values near pixel $x = 74$ (RA $= 17^{h}13^{m}44\overset{s}{.}49$) to near pixel $x = 103$ (RA $= 17^{h}13^{m}44\overset{s}{.}18$), and the line was interpolated to the position of the flux minimum near pixel $x = 83$ (RA $= 17^{h}13^{m}44\overset{s}{.}40$). The relative flux deficit to the interpolation was converted to an extinction value in magnitudes. This process was carried out for the same cut in the channel-1 short, medium, and long data cubes. For the other channels, the data cubes were resampled to the channel-1 pixel scale (0.13 arcsec pixel^{-1}) using the world coordinate system information for each cube, and then the same fitting process was carried out wavelength-by-wavelength for these nine resampled data cubes. This process provides a measurement of the wavelength-dependent extinction across the absorption band over the full MIRI wavelength range.

Fig. 9 shows the resulting wavelength variation of extinction. The figure also plots the dust mass absorption coefficient, κ, for model ISM grains (Weingartner & Draine 2001). Compared with standard ISM dust grains, the extinction curve for NGC 6302 is rather flat across the wavelength range, and the 10 μm silicate feature is rather weak. This may be explained by the presence of larger grains, typically micron-sized grains. Such an extinction curve is represented by 2 μm ISM grains, using the optical constants from Draine & Lee (1984). The small features around 10 μm are mainly due to crystalline enstatite and quartz, on top of the amorphous silicate. The features longward of 15 μm are due to crystalline enstatite, quartz, and forsterite.

Combining this relative extinction map with the wavelength dependence shown in Fig. 9 allows extinction estimates to be made across the central area of the nebula, under the assumption that the wavelength dependence is the same at all points in the central area. Further work is needed to assess how valid an assumption this is, but

together, these give an initial estimate of the extinction effects for the MIRI data.

5 DISCUSSION

5.1 Dust in the torus

5.1.1 The extinction mass of the dusty torus

The dense torus is notable, through its extinction, as a dark lane dissecting the visible nebula (Fig. 1). It is also seen in CO (Santander-García et al. 2016; this work) and in sub-mm dust continuum emission (Matsuura et al. 2005), both of which have the advantage of probing both the front and the back of the torus and the nebula, while extinction only allows the front to be seen. The torus contains a large fraction of the mass of the overall dust mass in NGC 6302. From the James Clerk Maxwell Telescope data, Matsuura et al. (2005) derive a torus dust mass of 0.03 $M_\odot$, or a total (gas + dust) mass of 3 $M_\odot$ assuming a canonical gas-to-dust mass ratio of 100.

The extinction map can be used to estimate a torus mass. The extinction at 5.9 μm can be converted to A_V using the extinction curve of Gordon et al. (2023), which gives $A(\lambda = 5.9\,\mu\text{m})/A(V) = 0.0261$ mag, where we assume $R_V = 3.1$. The value for A_V is then converted to a hydrogen column density using the relation of Güver & Özel (2009). The total mass is obtained by integrating the column density over the area.

With these assumptions, the area of the torus, defined as the region for which $A_{5.91\,\mu\text{m}} > 2.0$ mag (Fig. 8), that corresponds to $A(V) > 76.6$ mag with a standard ISM extinction curve (Gordon et al. 2023), Fig. 8 gives a total hydrogen mass of $M = 1.6\,M_\odot$. The method can only measure the torus mass in front of the nebula, and presumably the same amount is present behind the nebula. The total hydrogen mass becomes $M_{\text{torus}} \sim 3\,M_\odot$.

There are substantial uncertainties in this method. The conversion from extinction at 5.9 μm to A_V and the conversion from A_V to N_{H} both assume typical interstellar dust, whereas the dust in NGC 6302 may be different. While the dust mass absorption coefficient κ of astronomical silicates (Draine & Lee 1984) with a grain radius of 2 μm, and the Milky Way ISM dust with $R_V = 3.1$ (Weingartner & Draine 2001) are more or less the same at 5.9 μm (∼500 and 508 cm^{-2} g, respectively), the κ of silicates from Ossenkopf, Henning & Mathis (1992) is twice as high at a radius of 2 μm, hence the mass would be reduced by a factor of 2. The method also does not take into account asymmetric structure, which is expected from a warped torus: the dust extinction map captures the near side of the north of the torus, which also has the highest ^{13}CO intensity (Fig. 7). The derived mass should be viewed as indicative, with a potential range of 0.8–3 $M_\odot$.

Assuming that the line-of-sight depth of the dark lane is the same as its linear extent (5.5 arcsec, or 1.7×10^{17} cm), the hydrogen density of the dark lane is $n_{\text{H}} \sim 6 \times 10^6\,\text{cm}^{-3}$.

The ionized gas has the highest density at the central region, $n_{\text{e}} = 4 \times 10^4\,\text{cm}^{-3}$, with an electron temperature of $T_{\text{e}} = 1.90 \times 10^4$ K (Rauber et al. 2014). These values, measured from optical lines, would indicate approximate pressure equilibrium between the dense lane and the ionized gas if the gas temperature in the lane is $T \sim 100$ K.

5.1.2 Dust formation in the torus

The *ISO* detection of crystalline silicates, such as forsterite (Mg_2SiO_4) and enstatite ($MgSiO_3$), suggested that gas-phase condensation occurs close to chemical equilibrium in a disc or torus (Waters et al. 1998; Molster et al. 1999; Kemper et al. 2004; Nuth et al. 2006). The *ISO* detection of other minerals, such as diopside ($MgCaSi_2O_6$) in NGC 6302 (Kemper et al. 2002), supports this hypothesis and is reminiscent of the chemistry in planet-forming discs (e.g. Gail 1998; Sargent et al. 2009; Olofsson et al. 2010; Varga et al. 2024). For AGB stars in binary systems, a portion of the outflow may be trapped, so that it gains angular momentum and forms a disc or torus (Mastrodemos & Morris 1999; Mohamed & Podsiadlowski 2012). In such a binary disc, high densities and temperatures can be sustained for extended periods, persisting beyond the AGB phase and continuing through the post-AGB and PN stages. In contrast, these conditions of crystalline silicate formation are difficult to reconcile with a rapidly cooling AGB wind, where changes in pressure, temperature, and density occur faster than the time-scale required for chemical reactions. Consequently, most silicates in AGB outflows are amorphous, likely forming under non-equilibrium conditions (e.g. Cherchneff 2006), resulting in a predominantly glassy structure.

Previous observations of AGB stars, post-AGB stars, and PNe with *ISO* and *Spitzer* lacked the angular resolution necessary to distinguish between material in the stellar wind and that in the disc or torus (Matsuura et al. 2004; Gielen et al. 2009). Our spatially resolved observations with *JWST* MIRI definitely locate the crystalline silicate emission in the dense torus, providing strong confirmation of this scenario.

Furthermore, MIRI's detection of the large sizes of the dust grains suggests that dust formation occurs over an extended time-scale, allowing grains to grow to larger sizes.

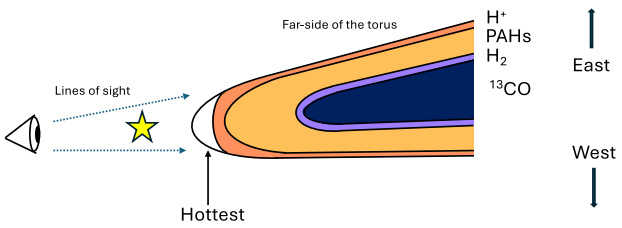

Figure 10. A schematic side-view image of the torus relative to the central star. The innermost region of the torus is filled with molecular gas, represented by ^{13}CO. As UV/X-ray radiation from the central star ionizes the gas, H^+, emission appears outside the ^{13}CO region. PAHs are found in the intermediate region between ^{13}CO and H I, while H_2 is likely located close to the ^{13}CO region.

5.2 The effects of photoionization on the torus

In the torus, a ^{13}CO traces the cold molecular region and extends north to south, and PAH emission is present on both sides of the ^{13}CO strip (Section 4.5.3; Fig. 7). The ionized hydrogen H I recombination line and H_2 emission appear adjacent to the ^{13}CO with a slight offset to the east (Fig. 7), whereas they overlap with the ^{13}CO on the west side. We attribute this stratification within the torus to a hierarchical PDR or X-ray-dominated region (XDR; Section 5.3) structure of different components within the torus, produced by the radiation from the central star. Projection of the torus structure towards our viewpoint causes such alignments progression of layers.

Fig. 10 shows a schematic picture of the far side of the torus from the side view, illustrating these alignments. The torus is slightly flared, and the scale height increases with a greater distance from the central star. The ^{13}CO is located at the innermost region of the torus in terms of the scale height. Due to the projection effect from the

observers point of view, the ^{13}CO lane runs in the middle of the torus in Fig. 7. The H^+, H_2, and PAHs are found on both side of the torus. The torus is viewed almost vertically edge-on on the western side, but slightly tilted to the east, hence all H^+, H_2, and PAHs are aligned on the western side. They are offset in the schematic picture (Fig. 10), but are not spatially resolved in the IFU reconstructed images, or the heavy dust extinction contained in the cold gas and dust region, traced by ^{13}CO, is obscuring the far radial end of the torus. The torus is slightly tilted on the eastern side from the observer's point of view, so that the flared part of the torus is spatially well resolved on the eastern side of the torus. The ^{13}CO emission is the mid-plane, and the inner edge of H^+ and H_2 follow, and PAHs are the outermost region. The H^+ and H_2 are extended from the inner edge to a higher scale height. The stratification of the eastern side of the torus is similar to that of the inner bubble.

It seems likely that some of the torus component is blown off by the hot bubble, contributing to ^{13}CO emission in the southern extent of the inner bubble.

When a torus is flared rather than flat, the central star can irradiate a higher scale height than in a flat case; if the torus is flat, UV radiation can reach only the inner radius of the torus, due to its extinction. This is well modelled for protoplanetary discs (Chiang & Goldreich 1997), where the flare is caused by hydrostatic and radiative equilibrium. The radiation from the central star reaches farther in the case of a flared disc, so that the emission, in projected view, is more extended on the eastern side of the torus from the observer's point of view. Henning et al. (2024) showed that, due to chemical reactions in the irradiated disc, different molecules can be found in different parts of the protoplanetary discs. That may occur in the torus of NGC 6302, too. In the case of H_2, this requires UV excitation from the central star; hence, it is only seen near the surface of the torus where there is little dust extinction. In contrast, the ^{13}CO excitation temperature could range from 20 to 35 K depending on the region (Peretto et al. 2007), so that it is in the inner, shielded regions inside of the torus (Fig. 10).

5.3 The expanding bubbles

Although the stratification of the ionized gas can largely be explained by photoionization, the presence of multiple H^+ edges and rims, along with the peanut-shaped structures and their interaction with the torus, suggests characteristics of a hot bubble surrounding a high-temperature central star.

The original concept of a hot bubble involves a hot ($\sim 10^6$ K) stellar wind colliding with the surrounding ISM or an AGB wind (Castor, Weaver & McCray 1975; Kwok, Purton & Fitzgerald 1978; Balick 1987). In the case of NGC 6302, the hot bubble is sweeping up material from the previously ejected nebula and the torus rather than from the ISM. The peanut-like shape of the H^+ rim (Section 4.4) suggests that the hot bubble blown by the wind is interacting with the torus at the intersection. While the bubble can continue to expand into lower density regions of the nebula, its expansion is stopped upon encountering the denser torus. This interaction causes the bubble to bend, resulting in its distinctive peanut-like morphology.

The structure of a hot bubble was modelled by radiative and hydrodynamic simulations. Toalá & Arthur (2016) calculated the effects when the fast (initially over 1000 km s^{-1}) wind from PN central star encounters the slowly expanding ($\sim$15 km s^{-1}) AGB material. This results in hot gas (over 10^6 K) at the centre with a gradual temperature decrease outwards. After about 1000 yr of interaction, instabilities develop, causing the formation of a filamentary structure of H^+ or a rim of compressed ionized gas, while the hotter gas still fills the interior. This morphological structure is well replicated in NGC 6302. Our *JWST*/MIRI observations show that emission lines from higher ionization potential species predominantly fill the region near the central star, while the sharp edges of hydrogen recombination line emissions encircle the hotter gas.

5.3.1 *Photoionization, shocks, and kinetic heating*

The stratification of ionized gas can be explained by two possible mechanisms: photoionization effects and kinetic effects. Since X-rays potentially contribute to both photoionization and the formation of a hot bubble, which generates shocks upon interacting with ambient material, we cannot determine which process primarily drives the stratification of ionized gas based on existing results alone.

First, we discuss the photoionization scenario. The hot (220 000 K) central star is capable of emitting from soft X-rays (100 eV $< h\nu <$ 1 keV) to far-UV (6 eV $< h\nu <$ 13.6 eV; Tielens & Hollenbach 1985; Wolfire et al. 2003) radiation (Wright et al. 2011), leading to the expectation that the highest ionization potential lines should be detected nearer the central star. For the case of a 220 000 K blackbody, 0.38 of all photons emitted have energies >54.4 eV capable of ionizing He^+ to He^{2+}, whereas only 0.00044 of all photons have energies >225 eV capable of ionizing Mg^{6+} to Mg^{7+}.[7] Mg^{7+} 3.028-μm emission has been detected, although not imaged, from the core of NGC 6302 by Casassus et al. (2000). The highest ion stages for which MRS imaging data are available are Si^{6+}, requiring 205 eV to create, and Mg^{6+}, requiring 187 eV to create. The 6.492- and 5.493-μm forbidden lines from these respective ions show comparable angular extents, which are both more compact than the extent of the He II 10–9 9.714-μm line (Fig. 6).

All five of the highly ionized species whose emission is imaged in Fig. 6 ([Si VII], [Mg VII], [Na VI], [Ar V], and [Mg V]) show a central hole. We attribute this lack of emission to the 'hole' containing more highly ionized ion stages of the respective species, e.g. ion stages from Mg^{7+} through to Mg^{12+} in the case of Mg. Only two of the ions whose emission is shown in Fig. 6 do not show the hole, namely H I 9–6 and He II 10–9. These arise from species that are already fully ionized, namely H^+ and He^{2+}, and so cannot be ionized further.

In the case of a hot bubble driven by stellar winds, hotter gas could still be present in the central hole, but an alternative possibility is present. As the hot bubble expands, sweeping up the surrounding nebular material, it generates shocks that locally increase the gas temperature. The temperature at these shock fronts could exceed the temperature of gas near the central star (Toalá & Arthur 2014). The high-temperature gas is enclosed by a thin rim of hydrogen recombination emission, as shock compression increases the local density while reducing the temperature (Toalá & Arthur 2014). Future investigations into the gas within this central hole will help determine whether photoionization or shocks from the hot bubble play a more dominant role in shaping the observed stratification.

The characteristics of PNe with a hot bubble are that they are young (a few thousand years old) and show X-ray emission. The bipolar

[7]For their nebular photoionization models, the best-fitting 220 000 K, log $g = 7.0$ H-deficient model atmosphere used by Wright et al. (2011) emits about a hundred times more photons with energies greater than 225 eV than a 220 000 K blackbody – see their fig. 5.

flows of NGC 6302 have an age of around 2000 yr (Szyszka et al. 2011; Balick et al. 2023), so it fits this picture. X-ray emission has not been detected in NGC 6302 (Montez et al. 2015). This might be because NGC 6302 is extended to *Chandra*. *Chandra* X-ray survey PNe tends to favour detections from compact sources (nebula radius smaller than 0.15 pc; Freeman et al. 2014), and NGC 6302 falls on this borderline. A deep X-ray exposure could test the presence of hot gas inside the bubble.

Of course, NGC 6302 experienced outflows in different directions, with historical outflows older than 2000 yr (Balick et al. 2023). These ionized gases overlay in projection and shape the overall butterfly nebula.

5.4 PAH formation or excitation exterior to the inner bubble

In the Orion Bar, *JWST* imaging and spectroscopy showed that the PAHs emission is located between the H^+ and H_2 layers. (Habart et al. 2024; Peeters et al. 2024). The situation in NGC 6302 is different, with PAH emission further from the H^+ rim and H_2 in the inner hot bubble. The environment appears to affect the relation between H_2 and PAHs. This may be related to excitation, PAH formation, or PAH destruction.

We can rule out the feasibility of PAH destruction by the hot bubble to explain the IR PAH emitting region in NGC 6302, based on the bonding energy argument. The ionization potential of H I is 13.6 eV and the binding energy of H–H in an H_2 molecule is 4.52 eV. Two major bonds in PAHs are C=C and C–H. The C–H bonds are rather fragile and Allamandola, Tielens & Barker (1985) mentioned an energy of 5 eV and above. The dissociation energy of a PAH is 4.6 eV (Micelotta, Jones & Tielens 2010). This is the dissociation energy by collisions, not by photoionization, so that careful comparison is needed. This PAH dissociation energy is more or less similar to the H_2 binding energy; however, the carbon cage of PAHs is more resilient to destruction, with a potential survival of up to 75 eV in collisional energy (Micelotta et al. 2010). The actual destruction is somewhere within this range (Micelotta et al. 2010). With this resilience of PAHs, it is easier to destroy H_2 than PAHs. Hence, PAHs could appear closer to the central star than H_2, if the physical conditions in the bubble had destroyed PAHs and H_2. The observed arrangement is different; hence, the destruction of PAHs by the physical conditions in the bubble is an unlikely cause of the H^+, H_2, and PAHs order of stratification at the bubble. This excludes the scenario in which PAHs were formed during the AGB or post-AGB phase and subsequently destroyed inside the inner bubble during the PN phase.

Instead, the observed stratification can be explained if the expanding hot bubble causes a radiative shock, with a shock front somewhere within or interior to the H I emitting region, where UV photons from the radiative shock trigger an UV-induced PDR structure in the pre-shocked region, forming the H^+ and H_2 stratification, followed by the UV-induced and potentially X-ray-induced chemistry and eventual PAH formation.

The sound speed of the bubble gas is approximately 16 km s^{-1}, assuming a temperature of 10 000 K and the density of 10^6 cm^{-3}. The assumed density is from the estimated electron density (Appendix A), and the temperature is estimated by Wright et al. (2011). In the H I emitting region, the temperature can be lower than that, hence, the sound speed can also be lower. With the expansion velocity of the gas of 13 km s^{-1}, measured from Br γ (Casassus et al. 2000), the hot bubble can exceed the sound speed, and can cause mild shocks. In the H I emitting region, the temperature can be lower than that, hence, the sound speed can also be lower. With the expansion velocity of the gas of 13 km s^{-1}, measured from Br γ (Casassus et al. 2000),[8] the hot bubble can exceed the sound speed, and can cause mild shocks.

Energy generated by shocks can produce radiation, and UV radiation from the shocked region can affect the temperature structure of the pre-shocked region, i.e. ahead of the shocks. Raymond (1979), Shull & McKee (1979), and Hollenbach & McKee (1989) examined the effect of the UV radiation from the shocked region on the pre-shocked (upstream) region. Shull & McKee (1979) showed that shock velocities higher than 110 km s^{-1} generate sufficient UV radiation in the upstream (pre-shocked region) to ionize the gas. Lower shock velocities will not ionize the gas (Allen et al. 2008), but still UV radiation from the shock front enters the neutral and the molecular H_2 region, if the pre-shocked region has a reasonably high density (McKee & Hollenbach 1980).

The spectrum of the radiation field can also have an effect. The central star of NGC 6302 is much hotter (2.2×10^5 K) and sufficient to generate soft X-ray emission. The exciting stars in the Orion star-forming region have temperatures of only 34 600 K (Abel, Ferland & O'Dell 2019). If the Orion Bar is a PDR, irradiated by UV, the difference in NGC 6302 could be due to X-ray radiation. Although X-rays have not been detected from NGC 6302, the hot (220 000 K) central star can emit soft X-rays and far-UV (fig. 5 in Wright et al. 2011). That can trigger an XDR (Wolfire, Vallini & Chevance 2022) in the ambient gas. Soft X-rays are predominantly shielded by hydrogen (Maloney, Hollenbach & Tielens 1996), so that relatively high density at the H^+ rim of the bubble might shield X-rays, and subsequently form H_2. An XDR can dissociate CO, leading to carbon chemistry (Meijerink & Spaans 2005), and PAHs formation (Woods et al. 2003). A PAH formation route through HCO^+ may benefit from X-ray irradiation (Woods et al. 2002). Indeed, HCO^+ has been detected in NGC 6302 (Moraga Baez et al., in preparation) and also CH_3^+ (Bhatt et al., submitted), which is also seeding carbon-rich chemistry. The CO emission has been detected at the H^+ rim of the inner bubble (Santander-García et al. 2016), and if X-ray radiation is strong enough to dissociate CO into C or C^+, it can open the route to form PAHs via HCO^+. A characteristic of XDRs is that the transition between H^+, H I, and H_2 is rather gradual as a function of hydrogen number density, compared with PDR. This transition in the bubble of NGC 6302 is much sharper than the one observed in the Orion Bar. This could be because the decline of the density at this rim is steep. The remaining question is why PAHs are detected far behind H_2 or HCO^+. PAHs can be excited by UV photons with energies larger than a few eV (Draine et al. 2021), which should be present in this region, hence, once PAHs are formed, they should be detected adjacent to the carbon chemistry region, i.e. HCO^+ and CH_3^+ (Berné et al. 2023), but PAHs are displaced behind these molecules. It might be because the time-scale of PAH formation is a slower process than

[8]Following deconvolution in quadrature for their instrumental FWHM resolution of 15 km s^{-1}, table 3 of Casassus et al. (2000) presents [Mg VIII] 3.028-μm FWHM line widths of 18 and 24 km s^{-1} for two orthogonal slit positions on the core of NGC 6302, along with Br γ FWHM values of 31 and 41 km s^{-1} at the same positions. Since each line width will have a contribution from thermal broadening, proportional to the square root of the ratio of the temperature divided by the mass of the species, as well as from macroscopic turbulent/expansion velocities, independent of the species mass, we can use these measured line widths for Mg and H to solve for the gas temperature and the macroscopic turbulent/expansion velocity. Using equations (1) and (2) of Barlow et al. (1995), we obtain temperatures of 24 000 and 42 000 K and corresponding turbulent/expansion velocities of 9.4 and 12.6 km s^{-1} for the two slit positions.

the formation of H_2. Detailed chemical and PAH excitation models would be needed to explain PAH formation behind this inner bubble.

The displacement of IR PAHs emitting regions relative to H_2 emitting region in PDR regions can be influenced by differing shielding mechanisms affecting H_2 and CO. This concept is applied to the star-forming region N13 in the Small Magellanic Cloud (SMC). Recent *JWST* observations reveal that H_2 and PAHs in N13 are co-located or that PAHs are slightly behind H_2 (Clark et al. 2025), contrasting with the Orion Bar, where PAHs are observed closer to the exciting star than H_2 (Habart et al. 2024; Peeters et al. 2024). The stratification observed in N13 is attributed to the fact that H_2 is capable of self-shielding (Maloney et al. 1996; Wolfire, Hollenbach & McKee 2010; Gnedin & Draine 2014), whereas CO depends on dust extinction for protection against UV radiation. In the low-metallicity environment of the SMC, dust extinction is reduced, allowing UV photons to penetrate deeper compared to regions in the Milky Way. However, H_2 self-shielding remains effective, even at low metallicity. As a result, the stratification order of H_2 and PAHs is reversed in the SMC star-forming region N13 compared to the Orion Bar. In the case of NGC 6302, the high effective temperature of its central star has to be considered, as it emits more energetic UV photons than the exciting star in the Orion Bar. However, dust processing in NGC 6302 may have reduced dust extinction at UV wavelengths, allowing deeper UV penetration and resulting in a stratification pattern similar to that observed in N13.

The interpretation of the hot bubble and UV irradiation of the upstream material applies to only the latest outflow (inner bubble). That region is strongly affected by the presence of the warped torus; hence, UV radiation can be easily shielded in certain directions (north–north-west and south–south-east). Stellar UV penetrates throughout the core and far into the larger nebula of NGC 6302, suggesting that there is no ionization front in the bubble (or near it) to absorb all of the stellar UV photons. Once PAHs are formed, stellar UV radiation can excite PAHs in the nebula, such as the outer bubble.

6 CONCLUSIONS

We have explored the heart of the extreme bipolar PN NGC 6302 using *JWST* MRS mapping of its IR spectrum at unprecedentedly high angular resolution. These new spectral maps provide the spatial distributions of nearly 200 emission lines of neutral atomic, ionic, and molecular species; PAH features; and crystalline and amorphous silicates. Combined with ALMA ^{13}CO and H30α, these atomic and molecular lines and dust features have revealed structures deep inside the dust-obscured region at the centre of the PN, providing fresh insight into the chemistry and shaping of this luminous, massive, prototypical bipolar PN.

NGC 6302 has a central expanding torus that contains dust grains within. The expanding torus, with approximate radius at IR wavelengths of 5.5 arcsec, or 5700 au, is the primary dust reservoir with a total dust plus gas mass of 0.8–3 $M_\odot$. Its mid-IR spectra show a high fraction of crystalline silicates and inferred μm-sized dust grains, in contrast to typical ISM grain size distributions (a few Å to 1 μm grain size; Weingartner & Draine 2001). Our observations support the hypothesis of an equilibrium chemistry in a disc to form crystalline silicates and large dust grains.

The wind from the PN central star appears to have proceeded as a sequence of bursts rather than via a continuous outflow, resulting in bubbles and arc filaments. This may be due to the infall of material from a disc formed by mass transfer from a close companion, which may supply the central star with accretion energy capable of producing intermittent outflows. The central region of the PN is not represented by steady-state mass loss, but by more dynamic and impulsive energetic outflows.

Inside the inner bubble, a stratification of ionized species is found. Species with higher ionization potentials are found to have a more compact distribution, while the lower ionization potential species are found to be more extended. This shows that both the UV/X-ray radiation energy from the central star and perhaps the kinetic energy of the hot bubble cause a higher degree of ionization in the innermost regions, which decreases towards the outside. When the bubble breaks, the outflowing material shocks and heats previously ejected material, producing [Fe II] and [Ni II] line emission seen as the north-west and south-east jets.

JWST and ALMA capture the most recent stage of the wind, which forms the inner bubble, and blows some material off the torus. The inner bubble should also trigger shocks when it interacts with the ambient circumstellar material, which presumably consists of past outflows. The shock emits UV radiation, which penetrates the external regions and excites the H_2 and PAH emission. This emitting region of PAHs is found outside of H_2, and that might suggest that PAHs are formed at the outer region of the bubble. This could be the first indication of capturing the PAH formation site in a PN, important for understanding PAH formation chemistry.

ACKNOWLEDGEMENTS

This work is based on observations made with the NASA/ESA/CSA *James Webb Space Telescope* (*JWST*). The data were obtained from the *Mikulski Archive for Space Telescopes* at the Space Telescope Science Institute, which is operated by the Association of Universities for Research in Astronomy, Inc., under NASA contract NAS 5-03127 for *JWST*. These observations are associated with program #1742.

This work has made use of data from the European Space Agency (ESA) mission *Gaia* (https://www.cosmos.esa.int/gaia), processed by the *Gaia* Data Processing and Analysis Consortium (DPAC, https://www.cosmos.esa.int/web/gaia/dpac/consortium). Funding for the DPAC has been provided by national institutions, in particular, the institutions participating in the *Gaia* Multilateral Agreement.

This study is based on the international consortium of ESSENcE (Evolved Stars and their Nebulae in the *JWST* era).

MM and RW acknowledge support from the STFC Consolidated grant (ST/W000830/1). MJB and RW acknowledge support from the European Research Council (ERC) Advanced Grant SNDUST 694520.

AAZ acknowledges funding through UKRI/STFC through grant ST/T000414/1.

HLD acknowledges support from grant JWST-GO-01742.004 and NSF grants 1715332 and 2307117.

JC and EP acknowledge support from the University of Western Ontario, the Canadian Space Agency (CSA)[22JWGO1-14], and the Natural Sciences and Engineering Research Council of Canada.

NCS acknowledges support from NSF award AST-2307116.

GCS thanks Michael L. Norman and the Laboratory for Computational Astrophysics for the use of ZEUS-3D. The computations were performed at the Instituto de Astronomía-UNAM at Ensenada.

PK acknowledges support from the Science Foundation Ireland/Irish Research Council Pathway programme under grant number 21/PATH-S/9360.

KEK acknowledges support from grant JWST-GO-01742.010-A.

FK and MT were partly supported by the Spanish program Unidad de Excelencia María de Maeztu CEX2020-001058-M, financed by MCIN/AEI/10.13039/501100011033.

JML was supported by basic research funds of the Office of Naval Research. RS's contribution to the research described here was carried out at the Jet Propulsion Laboratory, California Institute of Technology, under a contract with NASA, and partially funded by grant JWST-GO-01742.005-A from the STScI under NASA contract NAS5-03127.

This research made use of PHOTUTILS, an ASTROPY package for detection and photometry of astronomical sources (Bradley 2023). The MONTAGE[9] was used in PYTHON code to make false colour images, developed by Chawner et al. (2020). The MONTAGE project is funded by the National Science Foundation under grant number ACI-1440620, and was previously funded by the National Aeronautics and Space Administration's Earth Science Technology Office, Computation Technologies Project, under Cooperative Agreement Number NCC5-626 between NASA and the California Institute of Technology.

This work makes use of the ALMA data: ADS/JAO.ALMA#2012.1.00320.S. ALMA is a partnership of ESO (representing its member states), NSF (USA) and NINS (Japan), together with NRC (Canada), NSC and ASIAA (Taiwan), and KASI (Republic of Korea), in cooperation with the Republic of Chile. The Joint ALMA Observatory is operated by ESO, AUI/NRAO, and NAOJ.

DATA AVAILABILITY

JWST data are available from the *Barbara A. Mikulski Archive for Space Telescopes* (*MAST*; https://mast.stsci.edu). The DOI of the data from this specific observing program is 10.17909/s1rn-1t84 http://archive.stsci.edu/doi/resolve/resolve.html?doi = 10.17909/s1rn-1t84. Reduced images will be available by request to the authors.

REFERENCES

Abel N. P., Ferland G. J., O'Dell C. R., 2019, ApJ, 881, 130
Allamandola L. J., Tielens A. G. G. M., Barker J. R., 1985, ApJ, 290, L25
Allen M. G., Groves B. A., Dopita M. A., Sutherland R. S., Kewley L. J., 2008, ApJS, 178, 20
Argyriou I. et al., 2023, A&A, 675, A111
Ashley M. C. B., Hyland A. R., 1988, ApJ, 331, 532
Balick B., 1987, AJ, 94, 671
Balick B., Frank A., 2002, ARA&A, 40, 439
Balick B., Borchert L., Kastner J. H., Frank A., Blackman E., Nordhaus J., Baez P. M., 2023, ApJ, 957, 54
Barlow M. J., Crawford I. A., Diego F., Dryburgh M., Fish A. C., Howarth I. D., Spyromilio J., Walker D. D., 1995, MNRAS, 272, 333
Beintema D. A., Pottasch S. R., 1999, A&A, 347, 942
Berné O. et al., 2023, Nature, 621, 56
Bradley L., 2023, astropy/photutils: 1.8.0 (1.8.0). Zenodo. Available at: https://doi.org/10.5281/zenodo.7946442
Bradley L. et al., 2022, astropy/photutils: 1.5.0 (1.5.0). Zenodo. Available at: https://doi.org/10.5281/zenodo.6825092
Bushouse H. et al., 2023, JWST Calibration Pipeline (1.9.5). Zenodo. Available at: https://doi.org/10.5281/zenodo.7692609
CASA Team, 2022, PASP, 134, 114501
Casassus S., Roche P. F., Barlow M. J., 2000, MNRAS, 314, 657
Castor J., Weaver R., McCray R., 1975, ApJ, 200, L107
Chatzikos M. et al., 2023, Rev. Mex. Astron. Astrofis., 59, 327
Chawner H. et al., 2020, MNRAS, 493, 2706
Cherchneff I., 2006, A&A, 456, 1001
Chiang E. I., Goldreich P., 1997, ApJ, 490, 368
Chihara H., Koike C., Tsuchiyama A., 2007, A&A, 464, 229
Clark I. Y. et al., 2025, preprint (arXiv:2504.06247)
Cohen M., Barlow M. J., 2005, MNRAS, 362, 1199
Dere K. P., Del Zanna G., Young P. R., Landi E., 2023, ApJS, 268, 52
Dinh-V-Trung, Bujarrabal V., Castro-Carrizo A., Lim J., Kwok S., 2008, ApJ, 673, 934
Draine B. T., Lee H. M., 1984, ApJ, 285, 89
Draine B. T., Li A., Hensley B. S., Hunt L. K., Sandstrom K., Smith J. D. T., 2021, ApJ, 917, 3
Dwek E., 1998, ApJ, 501, 643
Evans D. S., 1959, MNRAS, 119, 150
Fabian D., Henning T., Jäger C., Mutschke H., Dorschner J., Wehrhan O., 2001, A&A, 378, 228
Foreman-Mackey D., Hogg D. W., Lang D., Goodman J., 2013, PASP, 125, 306
Freeman M. et al., 2014, ApJ, 794, 99
Gaia Collaboration, 2023, A&A, 674, A1
Gail H. P., 1998, A&A, 332, 1099
Gardner J. P. et al., 2023, PASP, 135, 068001
Gielen C., Winckel H. V., Matsuura M., Min M., Deroo P., Waters L. B. F. M., Dominik C., 2009, A&A, 503, 843
Gnedin N. Y., Draine B. T., 2014, ApJ, 795, 37
Gómez-Gordillo S., Akras S., Gonçalves D. R., Steffen W., 2020, MNRAS, 492, 4097
Goodman J., Weare J., 2010, Commun. Appl. Math. Comput. Sci., 5, 65
Gordon K. D., Clayton G. C., Decleir M., Fitzpatrick E. L., Massa D., Misselt K. A., Tollerud E. J., 2023, ApJ, 950, 86
Greenhouse M. A., Grasdalen G. L., Woodward C. E., Benson J., Gehrz R. D., Rosenthal E., Skrutskie M. F., 1990, ApJ, 352, 307
Greenhouse M. A., Feldman U., Smith H. A., Klapisch M., Bhatia A. K., Bar-Shalom A., 1994, in Courvoisier T. J.-L., Blecha A., eds, Proc. IAU Symp. Vol. 159, Multi-Wavelength Continuum Emission of AGN. Kluwer, Dordrecht, p. 447
Güver T., Özel F., 2009, MNRAS, 400, 2050
Habart E. et al., 2024, A&A, 685, A73
Henning T. et al., 2024, PASP, 136, 054302
Hofmeister A. M., Bowey J. E., 2006, MNRAS, 367, 577
Hollenbach D., McKee C. F., 1989, ApJ, 342, 306
Hummer D. G., Storey P. J., 1987, MNRAS, 224, 801
Icke V., 2003, A&A, 405, L11
Jones O. C. et al., 2023, MNRAS, 523, 2519
Kastner J. H., Moraga Baez P., Balick B., Bublitz J., Montez R., Frank A., Blackman E., 2022, ApJ, 927, 100
Kemper F., Molster F. J., Jäger C., Waters L. B. F. M., 2002, A&A, 394, 679
Kemper F., Vriend W. J., Tielens A. G. G. M., 2004, ApJ, 609, 826
Koike C. et al., 2000, A&A, 363, 1115
Koike C., Imai Y., Chihara H., Suto H., Murata K., Tsuchiyama A., Tachibana S., Ohara S., 2010, ApJ, 709, 983
Kwok S., Purton C. R., Fitzgerald P. M., 1978, ApJ, 219, L125
Lester D. F., Dinerstein H. L., 1984, ApJ, 281, L67
McKee C. P., Hollenbach D. J., 1980, ARA&A, 18, 219
Maloney P. R., Hollenbach D. J., Tielens A. G. G. M., 1996, ApJ, 466, 561
Mastrodemos N., Morris M., 1999, ApJ, 523, 357
Matsuura M. et al., 2004, ApJ, 604, 791
Matsuura M., Zijlstra A. A., Molster F. J., Waters L. B. F. M., Nomura H., Sahai R., Hoare M. G., 2005, MNRAS, 359, 383
Matsuura M. et al., 2009a, MNRAS, 396, 918
Matsuura M. et al., 2009b, ApJ, 700, 1067
Meaburn J., López J. A., Steffen W., Graham M. F., Holloway A. J., 2005, AJ, 130, 2303

[9]http://montage.ipac.caltech.edu/applications.html

Meaburn J., Lloyd M., Vaytet N. M. H., López J. A., 2008, MNRAS, 385, 269
Meijerink R., Spaans M., 2005, A&A, 436, 397
Micelotta E. R., Jones A. P., Tielens A. G. G. M., 2010, A&A, 510, A37
Min M., Hovenier J. W., Koter A. D., 2003, A&A, 404, 35
Mohamed S., Podsiadlowski P., 2012, Balt. Astron., 21, 88
Molster F. J. et al., 1999, Nature, 401, 563
Molster F. J. et al., 2001, A&A, 372, 165
Molster F. J., Waters L. B. F. M., Tielens A. G. G. M., 2002, A&A, 382, 222
Montez R. J. et al., 2015, ApJ, 800, 8
Murata K., Chihara H., Koike C., Noguchi T., Takakura T., Imai Y., Tsuchiyama A., 2009, ApJ, 698, 1903
Nuth J. A., III, Wilkinson G. M., Johnson N. M., Dwyer M., 2006, ApJ, 644, 1164
Olofsson J., Augereau J.-C., van Dishoeck E. F., Merín B., Grosso N., Ménard F., Blake G. A., Monin J.-L., 2010, A&A, 520, A39
Ossenkopf V., Henning T., Mathis J. S., 1992, A&A, 261, 567
Peeters E. et al., 2024, A&A, 685, A74
Péquignot D., Morisset C., Casassus S., 2012, in Manchado A., Stanghellini L., Schönberner D., eds, Proc. IAU Symp. Vol. 283, Planetary Nebulae: An Eye to the Future. Cambridge Univ. Press, Cambridge, p. 470
Peretto N., Fuller G., Zijlstra A., Patel N., 2007, A&A, 473, 207
Pignata R. A., Weidmann W. A., Schmidt E. O., Mudrik A., Mast D., 2024, MNRAS, 528, 459
Rauber A. B., Copetti M. V. F., Krabbe A. C., 2014, A&A, 563, A42
Raymond J. C., 1979, ApJS, 39, 1
Rieke G. H., Lebofsky M. J., 1985, ApJ, 288, 618
Rigby J. et al., 2023, PASP, 135, 048001
Roche P. F., Aitken D. K., 1986, MNRAS, 221, 63
Rodriguez L. F., Moran J. M., 1982, Nature, 299, 323
Roueff E., Abgrall H., Czachorowski P., Pachucki K., Puchalski M., Komasa J., 2019, A&A, 630, A58
Sahai R., Morris M. R., Villar G. G., 2011, AJ, 141, 134
Saito R. K. et al., 2012, A&A, 537, A107
Santander-García M., Bujarrabal V., Alcolea J., Castro-Carrizo A., Contreras C. S., Quintana-Lacaci G., Corradi R. L. M., Neri R., 2016, A&A, 597, A27
Sargent B. A. et al., 2009, ApJS, 182, 477
Shull J. M., McKee C. F., 1979, ApJ, 227, 131
Soker N., Kashi A., 2012, ApJ, 746, 100
Suto H. et al., 2006, MNRAS, 370, 1599
Szyszka C., Walsh J. R., Zijlstra A. A., Tsamis Y. G., 2009, ApJ, 707, L32
Szyszka C., Zijlstra A. A., Walsh J. R., 2011, MNRAS, 416, 715
Temim T. et al., 2024, ApJ, 968, L18
Tielens A. G. G. M., Hollenbach D., 1985, ApJ, 291, 722
Toalá J. A., Arthur S. J., 2014, MNRAS, 443, 3486
Toalá J. A., Arthur S. J., 2016, MNRAS, 463, 4438
Uscanga L., Velázquez P. F., Esquivel A., Raga A. C., Boumis P., Cantó J., 2014, MNRAS, 442, 3162
van Hoof P. A., 2018, Galaxies, 6, 63
Varga J. et al., 2024, A&A, 681, A47
Waters L. B. F. M. et al., 1998, Nature, 391, 868
Weingartner J. C., Draine B. T., 2001, ApJ, 548, 296
Wells M. et al., 2015, PASP, 127, 646
Wesson R., 2016, MNRAS, 456, 3774
Wesson R. et al., 2024, MNRAS, 528, 3392
Wolfire M. G., McKee C. F., Hollenbach D., Tielens A. G. G. M., 2003, ApJ, 587, 278
Wolfire M. G., Hollenbach D., McKee C. F., 2010, ApJ, 716, 1191
Wolfire M. G., Vallini L., Chevance M., 2022, ARA&A, 60, 247
Woods P. M., Millar T. J., Zijlstra A. A., Herbst E., 2002, ApJ, 574, L167
Woods P. M., Millar T. J., Herbst E., Zijlstra A. A., 2003, A&A, 402, 189
Wright N. J., Barlow M. J., Ercolano B., Rauch T., 2011, MNRAS, 418, 370
Wright G. S. et al., 2023, PASP, 135, 048003
Zeidler S., Posch T., Mutschke H., Richter H., Wehrhan O., 2011, A&A, 526, A68
Zeidler S., Posch T., Mutschke H., 2013, A&A, 553, A81
Zeidler S., Mutschke H., Posch T., 2015, ApJ, 798, 125

SUPPORTING INFORMATION

Supplementary data are available at *MNRAS* online.

Fe_jet3_slow

Please note: Oxford University Press is not responsible for the content or functionality of any supporting materials supplied by the authors. Any queries (other than missing material) should be directed to the corresponding author for the article.

APPENDIX A: ELECTRON DENSITY

There are three good density diagnostics: [Ar III] 8.99/21.83 μm, [Ar V] 7.9/13.1, and [Cl IV] 11.76/20.31 line ratios. From the integrated spectrum, these give electron densities of 35 000, 12 800, and 12 000 cm^{-3}, respectively – very similar to the values from optical diagnostics in the UVES (Ultraviolet and Visual Echelle Spectrograph) spectra of Péquignot, Morisset & Casassus (2012): 12 000, 16 000, and 16 000 cm^{-3} from [O II], [Cl III], and [Ar IV] density diagnostic ratios, respectively.

In the jet, the estimated electron densities are 6000, 10 000, and 20 000 cm^{-3} from the [Fe II] 17.94/6.72, 17.94/25.99, and 17.94/5.34 ratios, respectively (Temim et al. 2024).

APPENDIX B: MARKOV CHAIN MONTE CARLO FITTING TO SILICATE BANDS

Fig. B1 demonstrates the Markov chain Monte Carlo (MCMC) fitting used to estimate the fractions of amorphous and crystalline silicates. The fitting is performed using EMCCE, developed by Foreman-Mackey et al. (2013), based on the MCMC method (Goodman & Weare 2010). The figure shows the relative abundances, assuming amorphous silicates of 2 μm size.

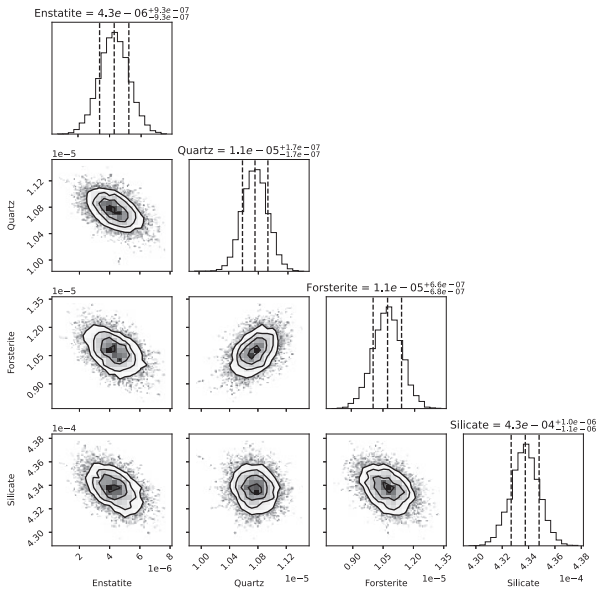

Figure B1. EMCCE fit to the spectra with four different dust compositions.

[1]*Cardiff Hub for Astrophysics Research and Technology (CHART), School of Physics and Astronomy, Cardiff University, The Parade, Cardiff CF24 3AA, UK*
[2]*Space Telescope Science Institute, 3700 San Martin Drive, Baltimore, MD 21218, USA*
[3]*Department of Physics, Maynooth University, Maynooth, Co Kildare, Ireland*
[4]*Department of Astronomy, University of Washington, Seattle, WA 98195-1580, USA*
[5]*Department of Physics and Astronomy, University College London, Gower Street, London WC1E 6BT, UK*
[6]*Jodrell Bank Centre for Astrophysics, Department of Physics & Astronomy, The University of Manchester, Oxford Road, Manchester M13 9PL, UK*
[7]*School of Mathematical and Physical Sciences, Macquarie University, Sydney, NSW 2109, Australia*
[8]*Department of Astronomy, University of Texas at Austin, Austin, TX 78712, USA*
[9]*Department of Physics and Astronomy, University of Western Ontario, London, Ontario, N6A 3K7, Canada*
[10]*Institute for Earth and Space Exploration, University of Western Ontario, London, Ontario, N6A 5B7, Canada*
[11]*SETI Institute, Mountain View, CA 94043 USA*
[12]*University of West Georgia, 1601 Maple Street, Carrollton, GA 30118, USA*
[13]*Center for Imaging Science, Rochester Institute of Technology, Rochester, NY 14623, USA*
[14]*School of Physics and Astronomy, Rochester Institute of Technology, Rochester, NY 14623, USA*
[15]*Laboratory for Multiwavelength Astrophysics, Rochester Institute of Technology, Rochester, NY 14623, USA*
[16]*European Southern Observatory, Karl-Schwarzschild Strasse 2, D-85748 Garching, Germany*
[17]*Department of Astrophysics/IMAPP, Radboud University, PO Box 19 9010, NL-6500 GL Nijmegen, the Netherlands*
[18]*SRON Netherlands Institute for Space Research, Niels Bohrweg 4, NL-2333 CA Leiden, the Netherlands*
[19]*Academia Sinica Institute of Astronomy and Astrophysics, 11F of Astronomy-Mathematics Building, AS/NTU, No. 1, Section 4, Roosevelt Road, Taipei 106319, Taiwan*
[20]*Laboratório Nacional de Astrofísica, Rua dos Estados Unidos, 154 Bairro das Nações, 37504-365 Itajubá, MG, Brazil*
[21]*ACRI-ST, CentredáEtudes et de Recherche de Grasse (CERGA), 10 Av. Nicolas Copernic, F-06130 Grasse, France*
[22]*INCLASS Common Laboratory, 10 Av. Nicolas Copernic, F-06130 Grasse, France*
[23]*Astronomy and Astrophysics Research Group, Department of Physics and Astrophysics, Vrije Universiteit Brussel, Pleinlaan 2, B-1050 Brussels, Belgium*
[24]*UK Astronomy Technology Centre, Royal Observatory, Blackford Hill, Edinburgh EH9 3HJ, UK*
[25]*Chalmers University of Technology, Onsala Space Observatory, SE-43992 Onsala, Sweden*
[26]*Institut de Ciències de l'Espai (ICE, CSIC), Can Magrans s/n, E-08193 Cerdanyola del Vallès, Barcelona, Spain*
[27]*ICREA, Pg. Lluís Companys 23, E-08010 Barcelona, Spain*
[28]*Institut d'Estudis Espacials de Catalunya (IEEC), E-08860 Castelldefels, Barcelona, Spain*
[29]*Institute for Scientific Research, Boston College, 140 Commonwealth Avenue, Chestnut Hill, MA 02467, USA*
[30]*Université Côte d'Azur, Observatoire de la Côte d'Azur, CNRS, Lagrange, 96 Bd de l'Observatoire, F-06300 Nice, France*
[31]*Space Science Division, Code 7684, Naval Research Laboratory, Washington, DC 20375, USA*
[32]*Leidse instrumentmakers School, Einsteinweg 61, NL-2333 CC Leiden, the Netherlands*
[33]*Instituto de Física e Química, Universidade Federal de Itajubá, Av. BPS 1303 Pinheirinho, 37500-903 Itajubá, MG, Brazil*
[34]*Jet Propulsion Laboratory, California Institute of Technology, 4800 Oak Grove Drive, Pasadena, CA 91109, USA*
[35]*Department of Physics and Astronomy, University of North Carolina, Chapel Hill, NC 27599-3255, USA*
[36]*Royal Observatory of Belgium, Ringlaan 3, B-1180 Brussels, Belgium*
[37]*Astrophysics Research Centre, Keele University, Newcastle ST5 5BG, UK*

This paper has been typeset from a TEX/LATEX file prepared by the author.